Full length article

The α→ω and β→ω phase transformations in Ti—Fe alloys under high-pressure torsion

A.R. Kilmametov [a], Yu. Ivanisenko [a], A.A. Mazilkin [a, b], B.B. Straumal [a, b, c, *], A.S. Gornakova [b], O.B. Fabrichnaya [d], M.J. Kriegel [d], D. Rafaja [d], H. Hahn [a]

[a] *Karlsruhe Institute of Technology (KIT), Institute of Nanotechnology, Hermann-von-Helmholtz-Platz 1, 76344 Eggenstein-Leopoldshafen, Germany*
[b] *Institute of Solid State Physics, Russian Academy of Sciences, Ac. Ossipyan str. 2, 142432 Chernogolovka, Russia*
[c] *National University of Science and Technology «MISIS», Leninskii prosp. 4, 119049 Moscow, Russia*
[d] *TU Bergakademie Freiberg, Institute of Materials Science, Gustav-Zeuner-Straße 5, 09599 Freiberg, Germany*

ARTICLE INFO

ABSTRACT

The formation of ω-phase under high-pressure torsion (HPT) has been studied in Ti—Fe alloys. Seven alloys with Fe concentration from 0 to 10 wt % have been annealed between 600 and 950 °C, quenched and HPT-treated at 7 GPa, 1 rpm, 5 and 0.1 anvil rotations (equivalent strain e_{eq} = 156 and = 3.1, respectively). The strain after 0.1 rot. corresponds to the transient state of HPT, and that after 5 rot. corresponds to the HPT steady-state and to the dynamic equilibrium between formation and annihilation of microstructure defects. A defect-rich high-pressure ω-phase forms after HPT and persists in the samples also after the pressure release. The amount of retained ω-phase after HPT depends on the iron concentration. It increases from 40% in pure titanium, reaches maximum of 95% at 4 wt % Fe and then decreases again to 10% at 10 wt % Fe. It is because the addition of iron influences the lattice parameters in β and ω-phases in a different manner. The minimal lattice mismatch between β- and ω-phases is reached at 4 wt % Fe. A good conformity between the lattices of the β- and ω-phases enhances the probability of the martensitic (diffusionless) β→ω transformation. Based on the XRD and TEM observations, the crystallography and mechanisms of α→ω and β→ω phase transformations (which can be diffusionless as well as controlled by mass transfer) under the influence of pure shear by HPT are discussed.

1. Introduction

Titanium-based alloys are very attractive for various applications due to their specific strength, high corrosion resistance and good biocompatibility [1]. One can apply the alloying, as well as various thermal and mechanical treatments of titanium alloys in order to tailor their structure and properties. Similar to iron, titanium has different allotropic modifications at high and low temperatures. This fact permits to develop a broad spectrum of thermal treatments technologies for the titanium-based alloys. Titanium also possesses a high pressure ω-phase. After pressure release the ω-phase can be observed as metastable one at ambient conditions [2,3]. In certain Ti-based alloys the metastable ω-phase can be produced without high pressure, just after a certain heat treatment [4—7].

The specific electronic structure facilitates the formation of ω-Ti. Namely titanium has the occupied narrow d-band and the broad sp-bands. Under the applied pressure, the sp-bands rise in energy and cause the electrons to be transferred into d-band [8]. This process is known as s-d transition and governs the structural properties of the transition metals. The elements stabilizing the β-phase in titanium are mostly transition ones (e.g. Nb, Cr, Zr, Fe, Ni, Cu, Co). They are rich on d-electrons. Thus, the alloying of titanium by the β-stabilizers increases the d-electron concentration. Such alloying can, therefore, provide an additional driving force for the α-Ti to ω-Ti transformation. For the α→ω phase transformation, one can consider the alloying of Ti with β-phase stabilizers as an equivalent of pressure. Hennig [9] concluded from *ab-initio* calculations that the alloying with β-stabilizing elements such as V, Mo, Fe or Ta should lead to a decrease in the onset pressure of the α→ω transformation. The combined effect of β-stabilizer alloying and pressure application (2—12 GPa) was experimentally studied using Zr—Nb, Ti—Nb and Ti—V alloys only in few works [10—12]. With

* Corresponding author. Institute of Solid State Physics, Russian Academy of Sciences, Chernogolovka, Moscow district, 142432 Russia.
E-mail address: straumal@issp.ac.ru (B.B. Straumal).

increasing concentration of β-stabilizer, the formation pressure of ω-Ti first decreases. Above a certain concentration of a β-stabilizer the formation pressure of ω-Ti rapidly grows.

Severe plastic deformation (SPD) can be considered as an alternative technology for improving the properties of Ti-based alloys. SPD always initiates the strong grain refinement [13] and can lead to various phase transitions [14]. Among them are formation of supersaturated solid solution [15—17] or those decomposition [18—22], dissolution of particles of a second solid phase [23—28], amorphization [29—34], nanocrystallization [35—37] etc. In many cases different SPD-driven phase transformations proceed simultaneously with each other and, therefore, can compete [21,38]. The phase transitions in Refs. [13—38] include mass-transfer and are, therefore, diffusive. It has been observed recently that SPD can induce displacive (or martensitic) phase transitions as well [39—43]. Sometimes they proceed simultaneously with diffusive ones [44]. The SPD-induced microstructure peculiarities of Ti and Ti-based alloys can cause their unique mechanical properties [45—47]. For example, SPD permits to achieve the extraordinarily combination of high strength and ductility in nanograined Ti [48,49]. Thus, SPD allows to improve the structure and properties of Ti-based alloys. The goal of this work is to study the SPD-driven α→ω and β→ω phase transformations in Ti-based alloys. Ti—Fe alloys were selected for this work as a typical example of the Ti-alloys with a so-called β-stabilizer. They exhibit an excellent combination of enhanced plasticity and high strength and are also useful for medical applications [50—52]. The high pressure torsion (HPT) is one of SPD techniques combining the high pressure with shear deformation. HPT permits to produce the high-pressure ω-phase in a number of Ti- and Zr-based alloys [45—47,53—55].

2. Experimental

In this work we studied pure titanium as well as titanium-iron alloys with 0.5, 1, 2.2, 4, 7 and 10 wt % Fe. All alloys were produced of high purity components (99.9% Ti and 99.97% Fe) using the inductive melting in high vacuum. The melt was poured in vacuum into the water-cooled cylindrical copper crucible of 10 mm diameter. After casting the samples were sawed, ground, and chemically etched. The resulted 0.7 mm thick disks were individually sealed in the evacuated silica ampoules with residual pressure of 4×10^{-4} Pa. The ampoules with samples inside have been annealed at $T = 950\ °C$, 104 h, $T = 800\ °C$, 270 h, $T = 680\ °C$, 550 h, $T = 620\ °C$, 270 h, $T = 600\ °C$, 1160 h and then quenched in water at room temperature (without breaking the ampoules). After these anneals the samples contained different amount of α- and β-phases, in turn, the β-phase contained different concentration of iron. The 2 mm thick slices were also cut from the ∅ 10 mm cylindrical ingots and then divided into four parts. These as-cast samples were embedded in resin and then mechanically ground and polished, using 1 μm diamond paste in the last polishing step, for the metallographic study. After etching, the as-cast samples were investigated by means of the scanning electron microscopy (SEM). Afterwards the thin disks were deformed by HPT in a Bridgman anvil type unit (at room temperature, pressure of 7 GPa, with the speed of 1 rotation-per-minute, for 0.1 and 5 rotations).

Torsion straining of a disc sample of diameter *2R* and thickness *t* produces a shear strain γ

$$\gamma = 2\pi\ n\ r/t, \tag{1}$$

n being the number of rotations of the mobile anvil, *r* being the distance from the sample centre. γ varies from zero on the sample axis to a maximum value γ_{max} on the lateral surface (situated at a distance $r = R$ from the axis). For comparison of shear deformation

with tensile strain, the equivalent strain value e_{eq} can be used [56,57]:

$$e_{eq} = \gamma\big/\sqrt{3} = 2\pi nr/t\sqrt{3} \tag{2}$$

All samples for the investigations were cut from the deformed disks at a distance of $r = 3$ mm from the sample centre. For this distance and 0.1 anvil rotations the shear strain $\gamma = 5.4$ and the equivalent strain value $e_{eq} = 3.1$. For 5 anvil rotations $\gamma = 270$ and $e_{eq} = 156$, respectively. This strain value has been typically used for the production of nanograined materials in earlier studies [18,56,57].

HPT was performed using a custom built computer-controlled device manufactured by W. Klement GmbH, Lang, Austria. Pure titanium was deformed in the as-cast state. The HPT machine permits to measure the torsion torque during HPT. The torsion torque increased during 1—2 anvil rotations in all alloys and pure Ti and then remained almost unchanged. In other words, it reached a steady state as it was observed previously in other alloys in Refs. [18—22,38,45]. The central part (about 3 mm in diameter) of each disk after HPT was excluded from further investigations (since it is low-deformed).

X-ray diffraction (XRD) patterns were measured in the Bragg—Brentano geometry in a powder diffractometer (Philips X'Pert) with Cu-Kα radiation. The Pseudo-Voigt function was used for fitting of XRD peak profiles. Lattice parameters were evaluated by the Fityk software [58] using a Rietveld-like whole profile refinement. Relative amounts of α-, β- and ω-phases were estimated from the integrated intensities. Pure polycrystalline titanium was used as reference. An empirical rule known as Vegard's rule (1921) was taken into account for subsequent analysis. SEM studies have been done using the Tescan Vega TS5130 MM microscope equipped with the LINK energy-dispersive X-Ray spectrometer (Oxford Instruments). Transmission electron microscopy (TEM) and high resolution TEM (HRTEM) observations have been made by using an aberration-corrected TITAN 80—300 transmission electron microscope. The cross section TEM and HRTEM specimens were cut from HPT discs at a 3 mm distance from the disc center. They were further thinned in a FEI Strata 400S dual beam facility. Automated Crystal Orientation Mapping (ACOM) TEM technique was used for phase mapping in the alloys after the HPT deformation. The ACOM TEM measurements were carried out on a Philips Tecnai F20ST operated at 200 kV in microprobe STEM mode. NanoMegas ASTAR system was used for ACOM-TEM data acquisition [59]. A primary electron beam with about 1 nm diameter and a convergence semi-angle of 1.4 mrad was generated. A camera length of 80 mm was used to acquire the diffraction patterns [60]. For indexing of the collected ACOM TEM diffraction patterns, we took the lattice parameters of the phases evaluated from the X-rays diffraction (XRD) data. Radial intensity distribution in ACOM TEM diffraction patterns was calculated using the ProcessDiffraction soft package [61].

3. Results

3.1. Influence of iron concentration

After anneals and quenching the seven studied alloys contained different amount of α- and β-phases as well as different concentration of iron in the β-phase. In the samples with low Fe-content (below 4 wt % Fe) annealed in the one-phase β-area and quenched, the martensite transformation of β-phase into α′ martensite takes place [62]. The respective orientation relationship (OR) between the lattices of β-Ti and α/α′-Ti is described as $(0001)_{\alpha}\big\|(110)_{\beta}; \langle11\overline{2}0\rangle_{\alpha}\|\langle111\rangle_{\beta}$ [63—71]. The Ti—4 wt % Fe alloy quenched from 950 °C contains almost 100% of undercooled β-
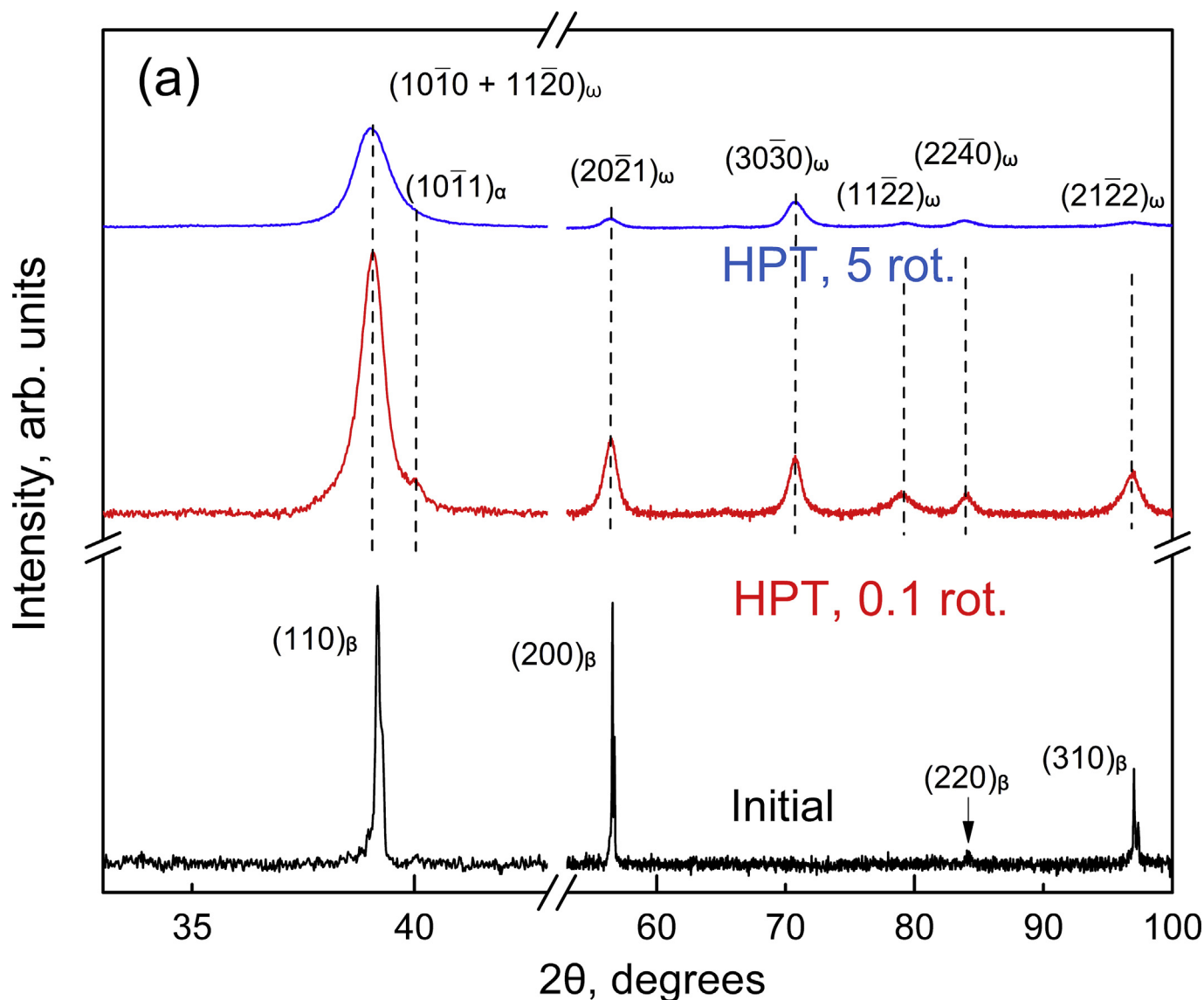
Fig. 1. The X-ray diffraction patterns of the Ti−4 wt % Fe alloy annealed at (a) $T = 950\ ^\circ$C for 104 h and (b) $T = 800\ ^\circ$C for 270 h in the state after annealing and quenching (bottom curves), after HPT at 7 GPa, 1 rpm, 0.1 rot (middle curves) and after HPT at 7 GPa, 1 rpm, 5 rot (upper curves). The patterns are vertically shifted for better comparison.

phase. All other annealed and quenched Ti−Fe alloys consist of the mixture of α/α′ and β-phases in different ratios. Moreover, the samples annealed in the two-phase α+β area of the Ti−Fe phase diagram contain the α-phase with almost zero concentration of iron and β-phase which accommodates the iron present in the individual sample. The annealed β-phase can contain up to 17 wt % Fe, according to the α-to-β transus line in the Ti−Fe phase diagram. In the samples annealed below transus line the α-phase forms short small stripe-like precipitates within the large grains. α-phase forms also continuous or discontinuous layers in β/β grain boundaries. These structures correspond to the complete or partial wetting of β/β GBs by a second solid phase α [45,72−74].

At the beginning of HPT treatment, the torsion torque quickly grows with the increasing number of anvil rotations. However, after 0.5−1 rotation it reaches certain saturation and slowly approaches a steady-state value. As one can expect, the Ti − 10 wt % Fe alloy is much stronger in comparison with pure Ti due to the solid solution or precipitation hardening in the alloyed titanium. The value of

steady-state torsion torque for Ti − 10 wt % Fe alloy (~500 N m) is much higher than that for pure titanium (~350 N m). Therefore, we investigated the structure of Ti−Fe alloys after HPT in two different states, namely "deep" in the steady-state after 5 anvil rotations (1800 deg., $e_{eq} = 156$) and at the very beginning of HPT treatment after 0.1 rot (about 30 deg., $e_{eq} = 3.1$).

Fig. 1 shows the XRD patterns for the Ti−4 wt % Fe alloy annealed at (a) $T = 950\ ^\circ$C, 104 h and (b) $T = 800\ ^\circ$C, 270 h after annealing and quenching before HPT (bottom plots), after HPT for 0.1 rot (middle plots) and after HPT for 5 rot (upper plots). The patterns are vertically shifted for better comparison. These samples were chosen as the most representative ones for the whole alloys family studied. The Ti−4 wt % Fe alloy annealed at $T = 950\ ^\circ$C and quenched (Fig. 1a, bottom curve) contained only β-phase with negligible amount of α′-martensite. The Fe content in the β-phase is equal to the total iron concentration in the whole sample, namely 4 wt % Fe. Sample Ti−4 wt % Fe annealed at $T = 800\ ^\circ$C and quenched (Fig. 1b, bottom curve) contained α-phase with almost
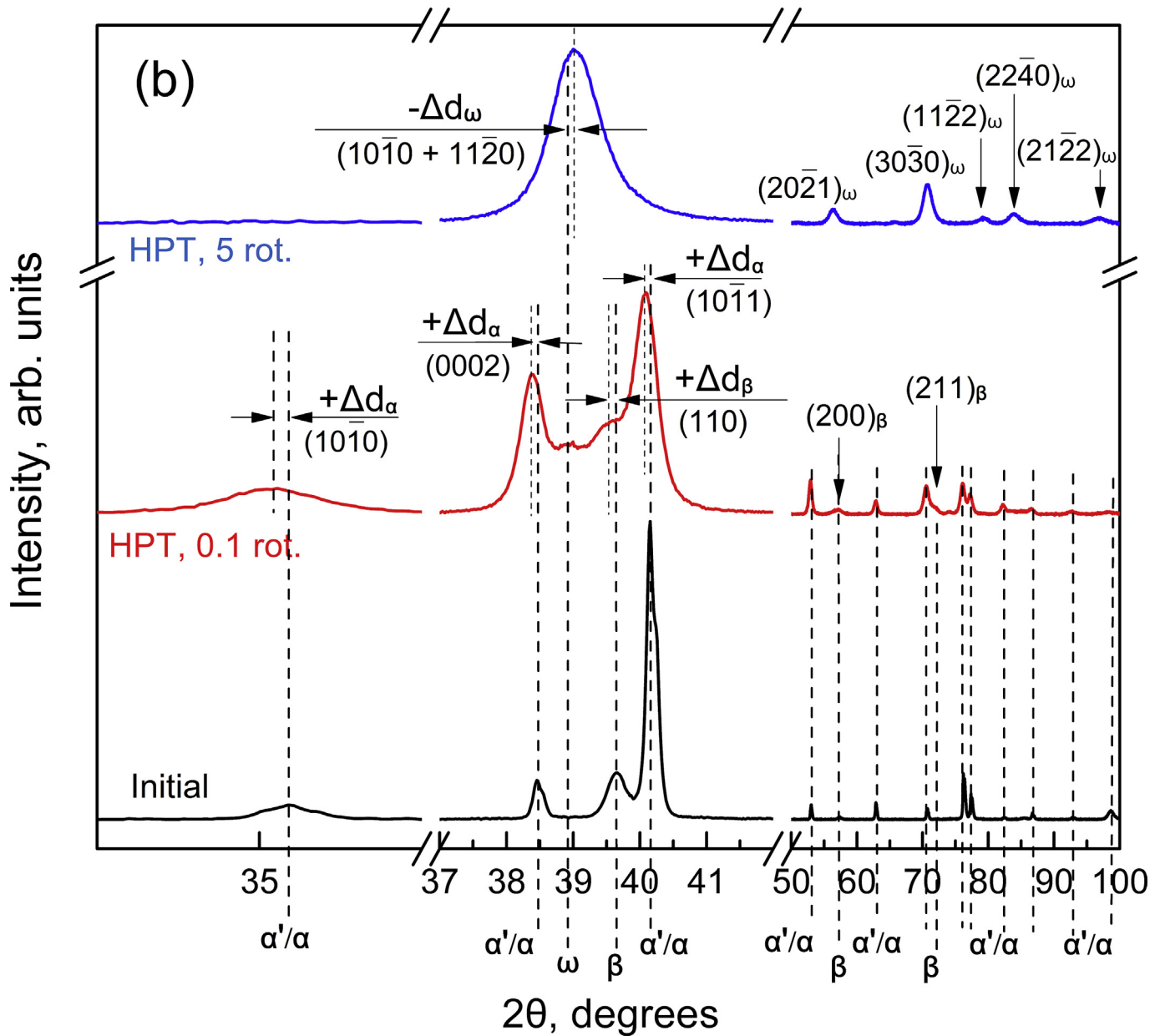
Fig. 1. (continued).

zero Fe content and β-phase with a high concentration of iron. The volume ratio of α- and β-phases (about 1:4) also corresponds to the phase diagram at 800 °C. Iron addition decreases the lattice constant of β-phase [75–78], therefore β-peaks in Fig. 1b (bottom curve) are shifted to the right in comparison with β-peaks in Fig. 1a (bottom curve).

The middle XRD pattern in Fig. 1a reveals that already after 0.1 rot., i.e. at much lower deformation than at steady-state one, β-phase completely disappears and ω-phase appears instead. As a result, a broad (101 + 110) doublet of ω-phase appears; it contains only a weak "shoulder" on the high-angle side (shown by the arrow) attributed to the rest of the α-phase. In contrast to the sample quenched from $T = 950$ °C (Fig. 1a), α- and β-phases are observed in the alloy quenched from $T = 800$ °C (Fig. 1b, bottom plot), and only a small amount of ω-phase forms after HPT for 0.1 rot. (see the weak peak around $2\theta = 39°$ between the peaks of α- and β-phases). The middle XRD pattern in Fig. 1b shows that β-phase still remains in

the sample after 0.1 rot. During HPT, the texture develops in the studied alloys. It apparently leads to the intensity redistribution among various XRD peaks. The intensity of the (002) peak for α-phase clearly increases as well as that of the (110) peak for β-phase. The upper curves in Fig. 1 show the XRD patterns after HPT for 5 rot., i.e. "deep" in the steady state. All the peaks are considerably broadened in comparison with the peaks of initial states (bottom plots in Fig. 1). This fact points towards a strong grain refinement and high defects density which are usual for HPT [2]. At the same time, XRD patterns for both states after HPT for 5 rot. look very similar. They contain about 90–95% of ω-phase with a very small amount of α- and/or β-phase.

Fig. 2a shows volume fraction of the ω-phase in the Ti–Fe alloys annealed at different temperatures after subsequent HPT treatment for 5 rot. The volume fractions of the ω-phase were determined from XRD data, basing on the analysis of the integrated intensities. The amount of ω-phase in pure titanium (transformed from the
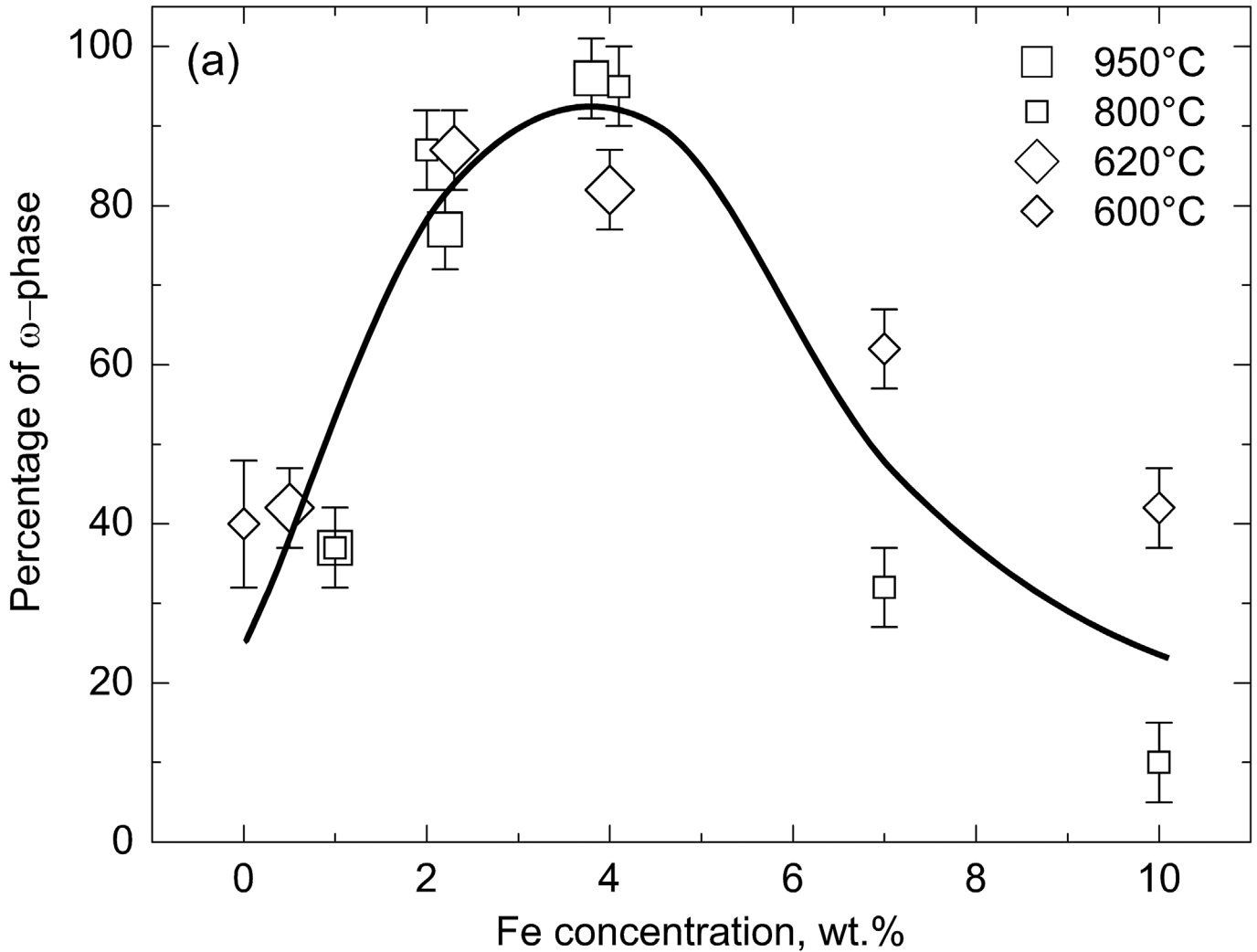
Fig. 2. (a) Percentages of the HPT-induced ω-phase in the Ti−Fe alloys having different Fe contents. Different symbols indicate different annealing temperatures prior to the HPT treatment. (b) Comparison of the lattice parameters a_ω measured in this work (filled circles) with the lattice parameters $\sqrt{2}\, a_\beta$ Ti−Fe alloys with different iron contents. For $\sqrt{2}\, a_\beta$, the values measured in this work (filled square) are given together with literature data (open triangles and circles [75−78]). Thin straight line shows the Vegard law for the β-phase and thick line shows that for the ω-phase. The Vegard lines for β- and ω-phases intersect at ~4 wt % Fe. (c) Dependence of cell density of ω-phase calculated from the X-rays data on iron concentration.

pure α-phase) is about 45%. The percentage of ω-phase grows up with increasing iron content and reaches maximum of about 95% at 4 wt % of iron (the remaining 5% is β-phase). A further increase of iron content reduces the volume fraction of ω-phase down to about 10% in the Ti − 10 wt % Fe alloy. It should be noted, that in the studied Ti − Fe alloys containing less than 4 wt % Fe the ω-phase is present together with α-phase. To the contrary, above 4 wt % Fe ω-phase coexists with β-phase and a negligible amount of α-phase. Due to the certain OR between the lattices of β- and ω-phases [4,6], the lattice parameters of hexagonal ω-phase can be expressed in terms of the lattice parameter of the bcc β-phase as: $a_\omega = \sqrt{2}\, a_\beta$ and $c_\omega = \frac{\sqrt{3}}{2}\, a_\beta$. Fig. 2b shows the comparison of the measured lattice parameters a_ω of the ω-phase (filled circles) and the calculated value $\sqrt{2}\, a_\beta$ (filled squares), where a_β is the measured parameter of the β-phase. All the primarily used values of lattice parameters have been derived from the full-profile X-ray analysis for the Ti−Fe alloys with different iron content (examples of such patterns are given in Fig. 1). In Fig. 2b, the lattice parameters $\sqrt{2}\, a_\beta$ measured in this work (filled squares) are compared with the literature data (open triangles and circles [75−78]). Thin straight

line shows the Vegard law for the β-phase and thick line shows the changes in lattice parameter for the ω-phase. These lines intersect at ~4 wt % Fe, that means that at 4 wt % Fe the best coincidence between lattices of β- and ω-phases along the lattice planes $(\{111\}_\beta \| (0001)_\omega ; \langle 1\bar{1}0 \rangle_\beta \| \langle 11\bar{2}0 \rangle_\omega)$ takes place. Lattice parameters of the ω-phase were used to calculate its atomic density in dependence on the iron content in the HPT treated Ti-Fe alloys. Fig. 2c shows the plot, where the atomic densities are presented as a number of atoms (in the primitive cell) per nm³. As known, the volume of hexagonal primitive cell is equal to $(\sqrt{3}/2)a^2 c$, where a and c are the lattice parameters, and the number of atoms in the ω-phase unit cell is three. One can see that atomic density of the ω-phase formed at the same HPT conditions after 5 rotations reaches a maximum at approximately 4 wt % Fe.

3.2. Structural details of α→β→ω transformations at 4 wt % Fe

The dark field TEM micrographs of the Ti−4 wt % Fe alloy (i.e. at the concentration maximum presented in Fig. 2) annealed at $T = 950$ °C, 104 h, quenched and subjected to HPT for 5 rot. are
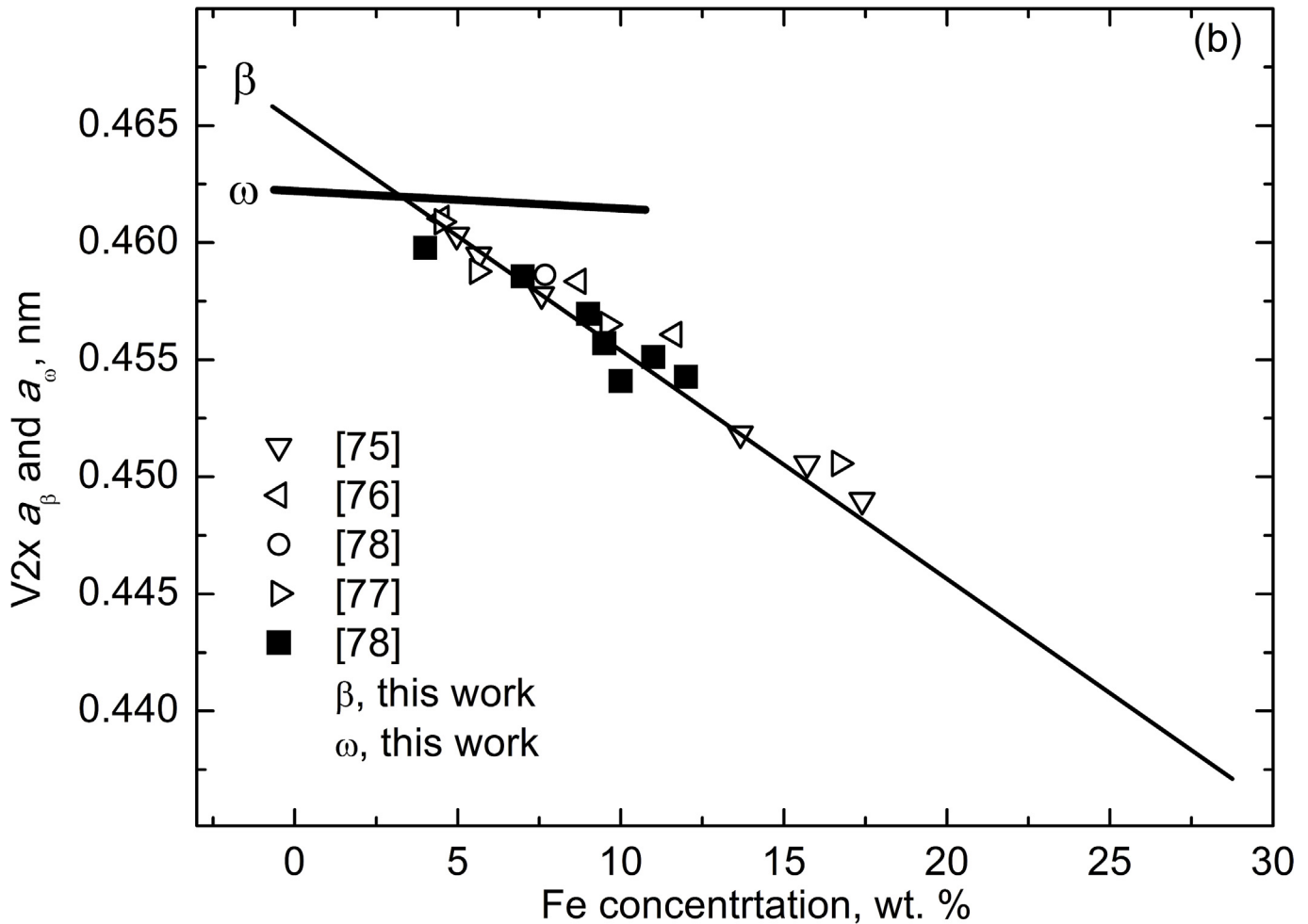
Fig. 2. (*continued*).

shown in Fig. 3. They demonstrate a very homogeneous structure with elongated fine grains with the size of 50—100 nm. The selected area diffraction pattern and the radial intensity distribution (inset in Fig. 3a and b, respectively) confirm that the sample does not contain any α-Ti phase. Fig. 3a shows that both titanium and iron are distributed in the sample very homogeneously (see the insets at the right side). Variations of contrast in the image are due to the different crystallite orientations.

Careful ACOM TEM inspection of the microstructure of the Ti—4 wt % Fe alloy annealed at $T = 950\,°C$, 104 h, quenched and subjected to HPT for 0.1 rot. has been done. It revealed interesting features shedding a light on the mechanism of the β→ω phase transformation. In the bright field image (Fig. 4a) three elongated grains represent a miniscule amount of the α-phase in the matrix of the β-phase. One of these particles is shown in the phase map calculated from the ACOM TEM data (Fig. 4b). The elongated particle is clearly defined as α-phase. It is surrounded by a thin "envelope" of the β-phase. The matrix around the "envelope" of β-phase consists of ω-phase. The elemental maps (Fig. 4b, insets) and point analysis reveal that α-phase (red) contains almost no Fe (0.07 ± 0.04 wt %), the β-phase (green) has about 9.6 ± 0.3 wt % Fe and ω-phase (blue) contains about 4.5 ± 0.2 wt % Fe.

In the left part of Fig. 5 the HRTEM image is shown for the same location in the sample as in Fig. 4b, namely for elongated α-grain (area 1) surrounded by a layer of β-phase (area 2) embedded in ω-matrix (area 3). In the right part of Fig. 5 the respective fast Fourier

transformations (FFT) of HRTEM image of electron diffraction patterns for α-phase (top, 1), β-phase (middle, 2) and ω-phase (bottom, 3) are shown. FFT from the area 1 corresponds to α-phase with normal direction (FN − film normal) along [132] axis. FFT from the area 2 corresponds to β-phase with normal direction along [110] axis. FFT from the area 3 (about 10 nm apart from the α-phase boundary) corresponds to different orientations of the ω-phase. Namely, it contains six possible orientations of the ω-phases, i.e. three with FN = [214] and three with FN = [100]. The first one matches the [110] diffraction pattern from β-phase. For two latter orientations, their two equivalent planes $(011)_\omega$ and $(01\bar{1})_\omega$ lie parallel to $g = (01\bar{1})_\beta$ of β-phase and give additional reflections in FFT. No special orientation relationship (corresponding to the known OR 1 $(0001)_\alpha \| (01\bar{1}1)_\omega; \langle 11\bar{2}0 \rangle_\alpha \| \langle 1\bar{1}01 \rangle_\omega$ and OR 2 $(0001)_\alpha \| (11\bar{2}0)_\omega; \langle 11\bar{2}0 \rangle_\alpha \| \langle 0001 \rangle_\omega$ [3,6]) between α and ω-phases was detected. However, martensitic relationship was appeared between β and ω phases: $\{111\}_\beta \| (0001)_\omega; \langle 1\bar{1}0 \rangle_\beta \| \langle 11\bar{2}0 \rangle_\omega$ [6,79].

3.3. Structural details of α→β→ω transformations at 2 wt % Fe

In Fig. 6 phase map from the ACOM TEM data (a) and elemental maps for two outlined areas (b) are shown for the Ti—2 wt % Fe alloy (i.e. below the concentration maximum presented in Fig. 2) annealed at $T = 800\,°C$, 270 h, quenched and subjected to HPT for 0.1 rot. The grain structure appears to be not very uniform. At the right side of the micrograph appear mainly β- and ω-phases. Here

Fig. 2. (*continued*).
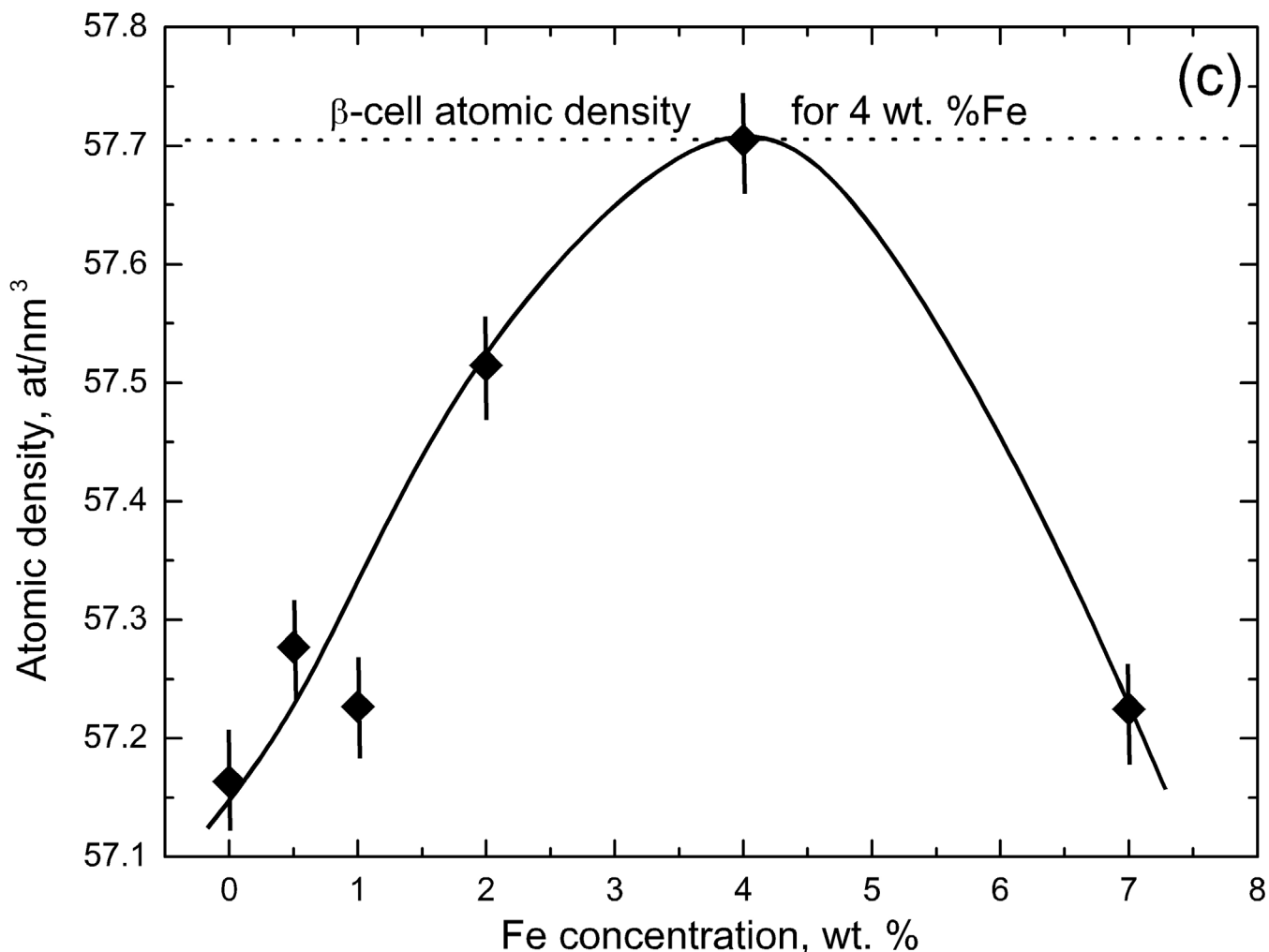
the grains are almost equiaxial. Oppositely, at the left side, the alternating grains of α-, β- and sometimes ω-phases are visible. All of them are elongated. The new ω-phase appears in the Fe-rich area, where the β-phase was located in the sample before HPT (see the inset corresponding to the area 1). The ω-phase is also observed in a broad area where the α-phase was located before HPT (see the inset corresponding to the area 2).

It follows from Fig. 6 that different ω-regions found in this sample have two different concentrations of iron. Most likely, the ω-phase transformed from the β-phase contains more iron. Respectively, the ω-phase transformed from the α-phase contained less iron. Before HPT, the α-phase had almost no iron, whereas the ω-phase transformed from the α-phase contains about 1—2 wt % Fe. At the same time, β-phase before HPT had about 7—8 wt % Fe, and the respective ω-phase transformed from the β-phase contains about 5—6 wt % Fe. In the steady state after 5 anvil rotations the concentration of iron is uniform in all samples and is equal to the nominal one of 2 wt % Fe.

Fig. 7 shows the HRTEM micrographs and FFT patterns of the Ti—2 wt % Fe alloy annealed at $T = 800$ °C, 270 h, quenched and subjected to HPT for 0.1 rot. In the left part of Fig. 7a the border area between the grains of two phases is visible. FFT patterns are for the right grain (top FFT) and for the left one (bottom FFT). We indexed the upper FFT belonging to α-phase and having the FN = [$11\bar{2}$ 0].

Microtwins are observed in the structure of α-grain, which cause the presence of numerous additional reflections along the [001] direction in the FFT pattern. The bottom FFT pattern can be indexed both as β-phase (with FN = [001]) and ω-phase (three equivalent orientations with FN = ⟨$0\bar{1}$ 12⟩). Therefore, we use here this type of parentheses instead of square brackets (as for the top FFT) to underline three equivalent orientations of ω-phase. The simulated diffraction patterns practically match each other, but in the FFT one can see that each individual spot is split. Most probably, this is the ω-grain formed during α→ω phase transformation. It contains several "subgrains" of three equivalent orientations mentioned above, producing the misorientation visible in FFT. The mutual arrangement of crystal lattices between grains does not correspond to the martensitic Pitsch-Schrader (PS) orientation relationship [63—71] but corresponds to the known OR 1 $(0001)_α \| (01\bar{1}1)_ω; \langle 11\bar{2}0 \rangle_α \| \langle 1\bar{1}01 \rangle_ω$ [3,6].

Along with grains of α- and ω-phases, which obey OR 1 and make up most of the sample, we observed also those without any rational OR. The example for that is Fig. 7b. Grains of α- and ω-phases are in contact. From the corresponding FFTs we can index the normal orientation for these grains. They are FN = [241] for α-Ti, and FN = [011 3] for ω-Ti. The crystal lattices of these two grains do not belong to any special OR.
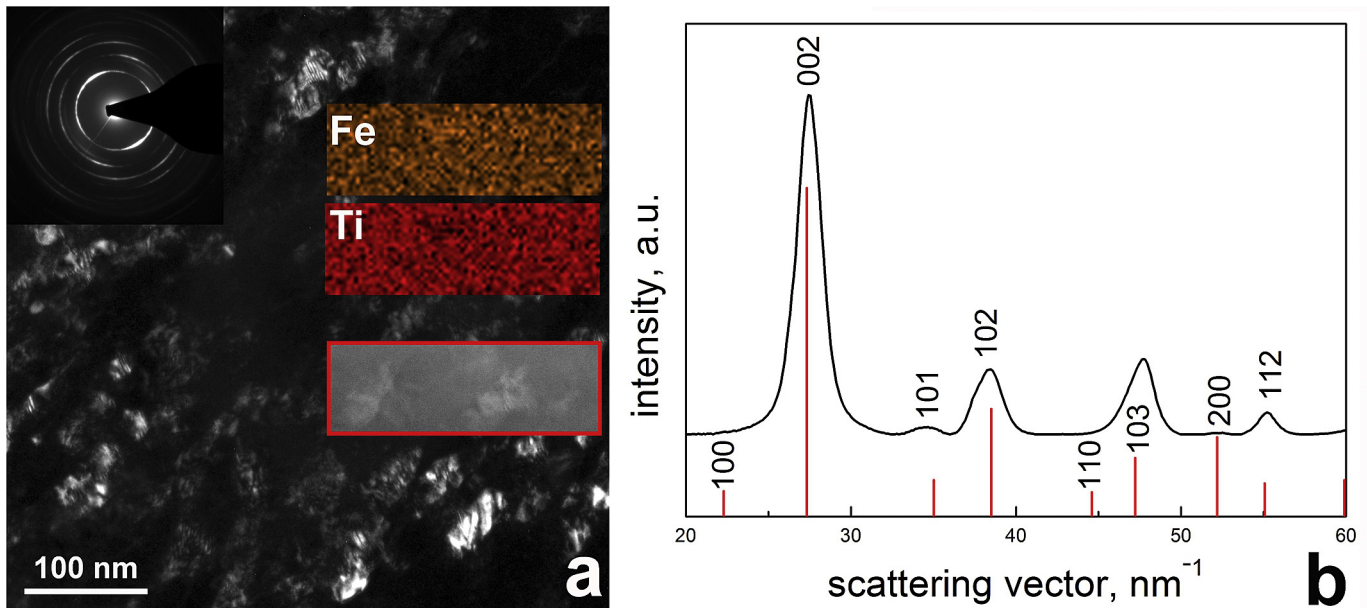
Fig. 3. Transmission electron micrograph and electron diffraction pattern of the Ti—4 wt % Fe alloy annealed at $T = 950$ °C, 104 h, quenched and subjected to HPT at 7 GPa, 1 rpm, 5 rot. (a) dark field image. The insets in Fig. 6a show: selected area electron diffraction pattern (upper left corner), part of the STEM HAADF image from the same sample's area (red outlined) and respective X-ray maps of Ti and Fe; (b) radial intensity distribution respective to the diffraction pattern. Red bar charts show the positions of the reflections from ω-Ti. Intensities were integrated along the Debye rings. (For interpretation of the references to colour in this figure legend, the reader is referred to the web version of this article.)
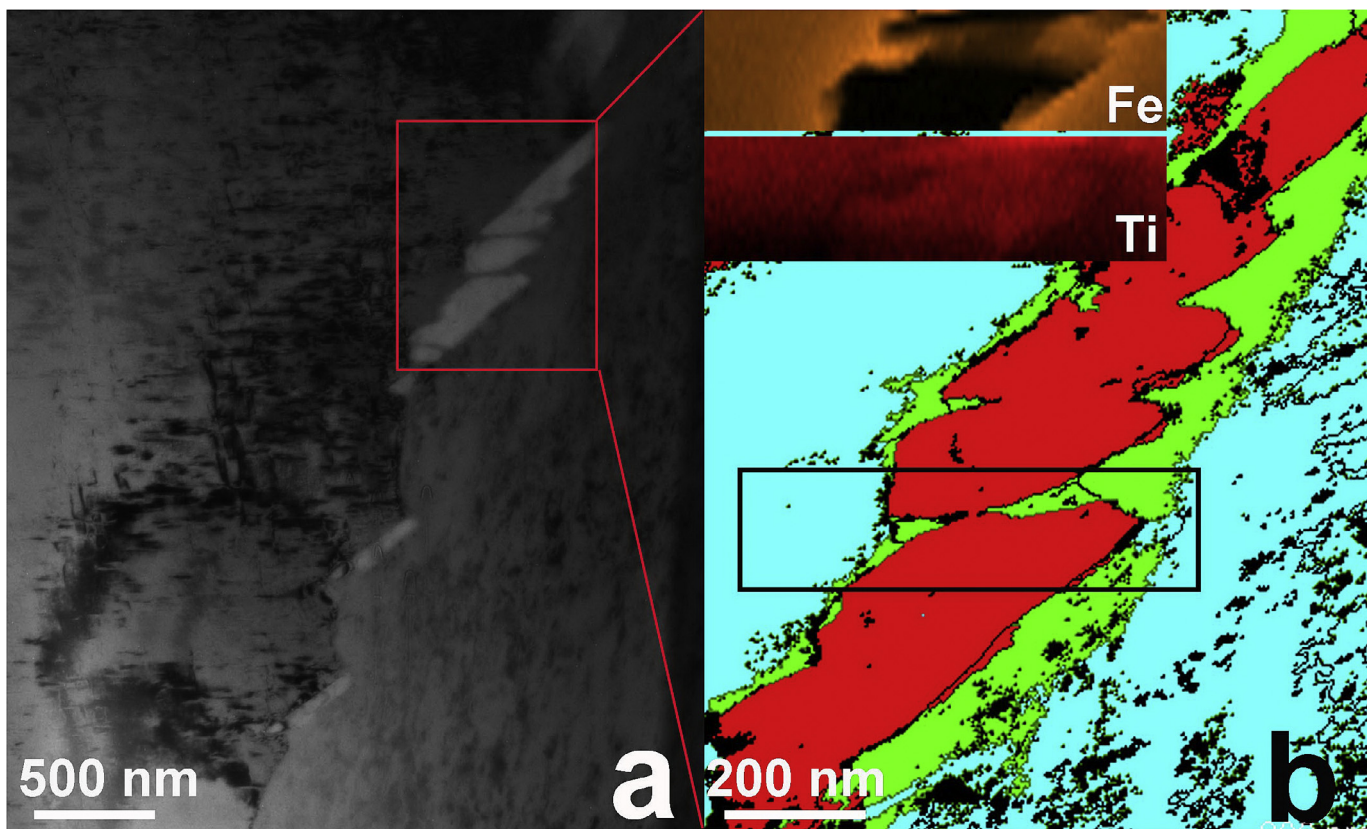
Fig. 4. Microstructure of the Ti—4 wt % Fe alloy annealed at $T = 950$ °C, 270 h, quenched and subjected to HPT at 7 GPa, 1 rpm, 0.1 rot. (a) bright field image, (b) phase map of a part of (a). Colours show different phases: α-phase is red, β-phase is green, ω-phase is turquoise. The black rectangle shows the field for elemental analysis. Respective maps of the intensities of the X-ray spectral lines of Ti and Fe are shown in the insets in Fig. 4b. (For interpretation of the references to colour in this figure legend, the reader is referred to the web version of this article.)
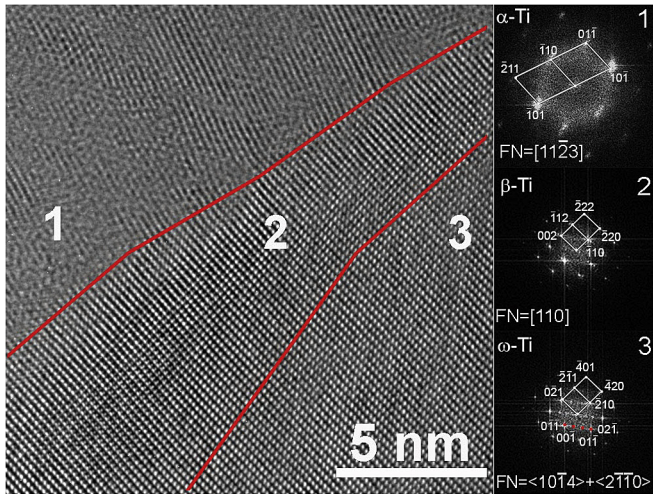
Fig. 5. (a) HRTEM micrograph of the Ti–4 wt % Fe alloy annealed at $T = 950\ ^\circ$C, 270 h, quenched and subjected to HPT at 7 GPa, 1 rpm, 0.1 rot. Same place as in Fig. 7 is shown, namely the elongated α-grain surrounded by a layer of β-phase embedded in ω-matrix. Corresponding FFTs are shown for α (1), β (2) and ω-phases (3). In region (3), the section of the reciprocal lattice with FN = [214] is shown by rectangular network; reflections originated from the section with FN = [100] are indicated by the red full circles. (For interpretation of the references to colour in this figure legend, the reader is referred to the web version of this article.)

4. Discussion

4.1. Influence of shear strain on the α → ω phase transformations

According to the literature [6,63–71], various orientation relationships exist between α, α′, β and ω phases. β- and α′-phases: $(0001)_\alpha\|(110)_\beta; \langle11\bar{2}0\rangle_\alpha\|\langle111\rangle_\beta$ [63–71]; β- and ω-phases: $\{111\}_\beta\|(0001)_\omega; \langle1\bar{1}0\rangle_\beta\|\langle11\bar{2}0\rangle_\omega$ [6,71]; α- and ω-phases: OR 1 $(0001)_\alpha\|(01\bar{1}1)_\omega; \langle11\bar{2}0\rangle_\alpha\|\langle1\bar{1}01\rangle_\omega$ and OR 2 $(0001)_\alpha\|(11\bar{2}0)_\omega;$

$\langle11\bar{2}0\rangle_\alpha\|\langle0001\rangle_\omega$ [3]. These ORs make commensurate the lattices of phases before and after phase transition. They make also possible the martensitic mechanism of transition, just by shear, i.e. without diffusive mass-transfer.

As was published earlier [46], noticeable deformation texture develops in the α-phase under HPT influence, namely the increased amount of basal atomic layers of the α-phase are oriented parallel to the specimen plane. In turn, the specimen plane coincides with the shear plain at HPT. Fig. 1b demonstrates significant increase of the intensity of XRD (002) peak even after 0.1 rot that accompanied with the appearance of the ω-phase. This fact is consistent with the theoretical prediction that α→ω transformation results from atomic shuffles in $(0001)_\alpha$ planes [80,81]. It is because the maximal shear stress acting in these $(0001)_\alpha$ planes under HPT facilitates the transformation. The formation of the basal texture in the α-phase prior to its transformation to the ω-phase allows us to expect that the new ω-grains also have preferential orientations according to the existing ORs between α- and ω-phases. The conclusion based on the XRD data concerning the texture formation in Ti alloys under the HPT deformation is supported by ACOM TEM measurements. Using the software, we calculated the pole figures (PFs) for the sample of the Ti–2 wt % Fe alloy subjected to HPT for 0.1 rot. The (0002) PFs for α and ω-Ti phase are shown in (Fig. 6c).

We compared obtained PFs with those which were measured and calculated for α-Ti [82] and ω-Ti [83,84] under the conditions of shear deformation. The PF for α-Ti has a somehow broadened but distinct poles corresponding to the basal slip system (B, $(0001)\langle11\bar{2}0\rangle$) and the basal plane of α-phase is parallel to the shear plane in the sample. The PF for ω-Ti indicate the presence of pyramidal slip in this phase (slip system P, $\{10\bar{1}0\}\langle1\bar{2}10\rangle$). Mutual activity of these two slip systems leads to the formation of aforementioned OR between α and ω phases. Example of this OR in the sample of Ti-alloy subjected to HPT deformation is shown in Fig. 7a. Thus, shear strain makes easier the α→ ω phase transformations.
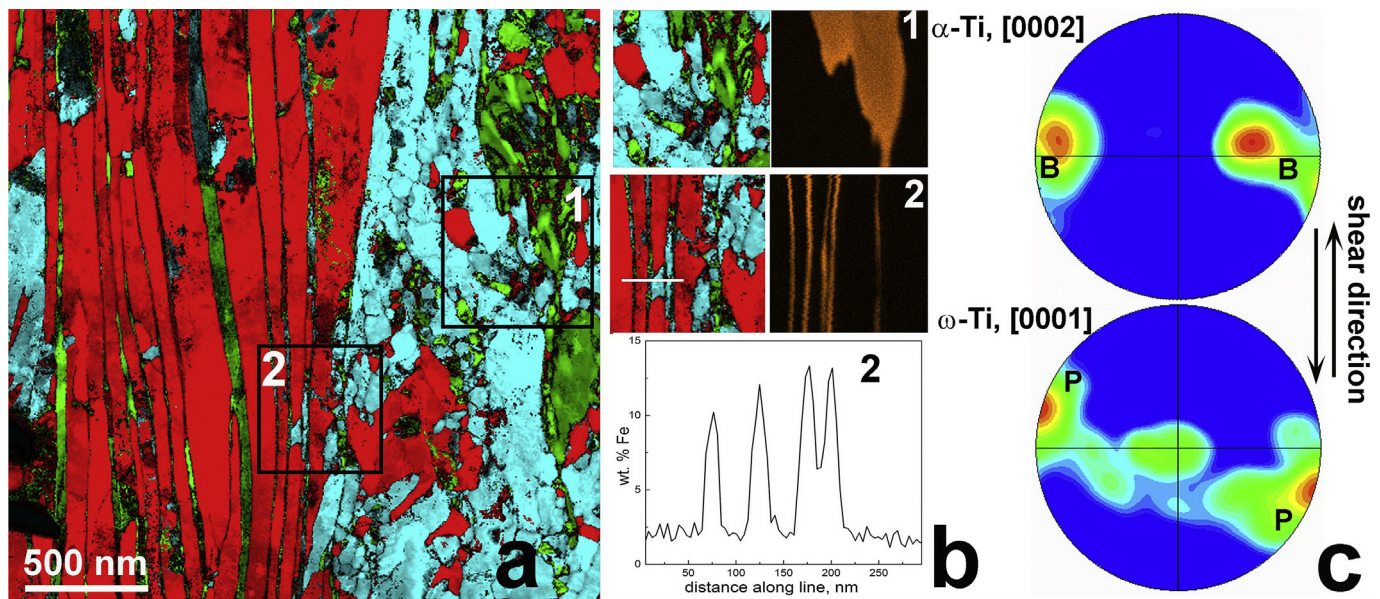
Fig. 6. Microstructure of the Ti–2 wt % Fe alloy annealed at $T = 800\ ^\circ$C, 270 h, quenched and subjected to HPT at 7 GPa, 1 rpm, 0.1 rot. (a) Phase map, colours show different phases: α-phase is red, β-phase is green, ω-phase is turquoise. (b) The EDX Fe map of two rectangle areas in (a); corresponding Fe concentration profile along the white line is shown beneath. (c) (001) PFs for α-Ti (top) and ω-Ti (bottom). The letters B and P denote the poles for basal $(0001)\langle11\bar{2}0\rangle$ and pyramidal $\{10\bar{1}0\}\langle1\bar{2}10\rangle$ slip systems. (For interpretation of the references to colour in this figure legend, the reader is referred to the web version of this article.)
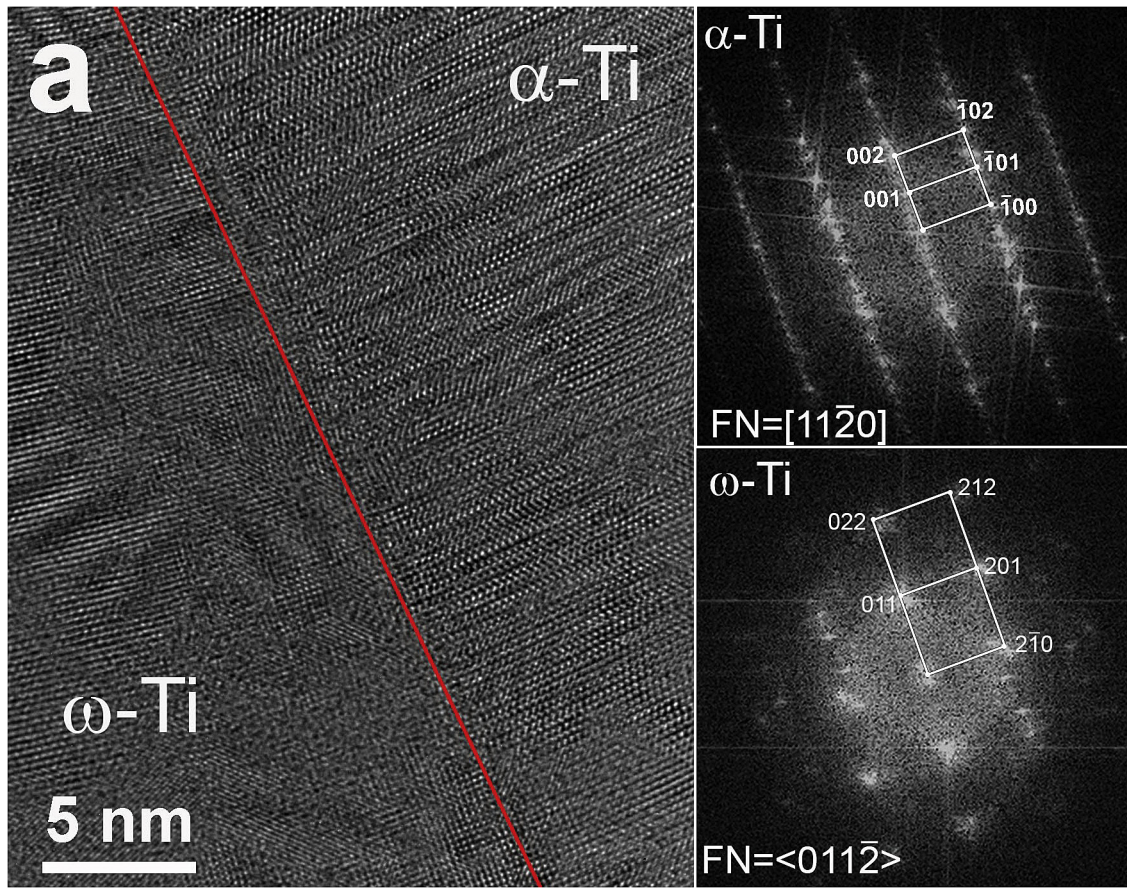
Fig. 7. HRTEM micrograph of the Ti−2 wt % Fe alloy annealed at $T = 800\,°C$, 270 h, quenched and subjected to HPT at 7 GPa, 1 rpm, 0.1 rot. (a) Mutual orientation of these two α and β grains correspond to the OR1, i.e., $(0001)_\alpha \| (01\bar{1}1)_\omega ; \langle 11\bar{2}0 \rangle_\alpha \| \langle 1\bar{1}01 \rangle_\omega$; (b) the orientation relationship between α and ω phases does not match any known special relationship.

4.2. Influence of the iron content on the β→ω phase transformation

At the moment only few experiments exist showing that the alloying of titanium can strongly influence the behavior of α→β→ω phase transformations under HPT [45,54,85]. In the Ti−10 wt %Fe alloy the β→ω transition has been significantly suppressed due to high concentration of iron in the solid solution [45]. This fact correlates with the results presented in the given work (Fig. 2a). For the case of lower doping, a number of Ti−Fe samples annealed and quenched at different temperatures are represented mostly as a mixture of (α/α'+β) phases. Here, α' is a hcp martensite (space group P6₃/mmc), which can be produced from β-phase at high cooling rate and low concentrations of β-stabilizing elements in titanium alloys [86−91]. The α-Ti and α'-Ti martensite belong to the same space group. Therefore, their XRD patterns of are very similar. Nevertheless, the XRD patterns of α-Ti and α'-Ti phases can be distinguished using the measurements of lattice parameters [92]. According to X-ray analysis, α'- martensite can be observed in the Ti−Fe alloys up to 4 wt % of iron. Its presence depends on the annealing temperature and the rate of the subsequent quenching. The maximal volume fraction of α'- martensite is reached between 0.5 and 1 wt % Fe [62]. As a result, in the steady state (after 5 HPT rotations) the transformation (α/α'+β) → (ω+α) takes place up to 4 wt%Fe with substantial increase of the ω-phase volume fraction (Fig. 2a).

The addition of iron to titanium decreases the lattice parameter of β-phase (Fig. 2b, plotted as $\sqrt{2}\,a_\beta$). The lattice parameter a_ω of ω-phase also decreases with increasing content of iron (Fig. 2b).

However, the decrease of lattice parameter a_ω is less pronounced than the reduction of the lattice parameter of β-Ti. As a result, both plots intersect at ~4 wt % Fe. It means that the orientation relationship between lattices of β- and ω-phases and conditions of formation of commensurate ω-phase fulfills in the best way at ~4 wt % Fe: $\{111\}_\beta \| (0001)_\omega ; \langle 1\bar{1}0 \rangle_\beta \| \langle 11\bar{2}0 \rangle_\omega$

This is the reason why the maximum portion of ω-phase after HPT of almost 100% is reached at 4 wt % Fe (Fig. 2a). The portion of ω-phase after HPT is lower than 100% at iron content below and above 4 wt % Fe. Below 4 wt % of Fe the samples after HPT contain ω-phase and α-phase. The solubility of Fe in α-phase is negligible. It means that the iron concentration in ω-phase is higher than that in the whole sample. It tends to be closer to the optimal concentration of 4 wt % Fe providing the smallest misfit between the β and ω lattices. On the contrary, the samples with the Fe content above 4 wt % Fe contain ω and β phases after HPT with some traces of α phase. The β-phase in such samples has more iron than the alloy in average. It means that ω-phase contains less iron than the sample in average, and the composition of ω-phase approaches the optimal iron concentration of 4 wt % Fe for the best β/ω lattice coincidence. It should be noted that the lattice parameter of β-phase in all samples after HPT tends to be slightly increased. This fact gives the evidence of the HPT-induced decreasing of Fe content in β-phase matrix. Thus, the addition of iron changes the lattice matching between β and ω grains and makes easier the β→ω phase transformations in comparison with pure Ti. The best matching between β and ω lattices is at 4 wt % Fe.
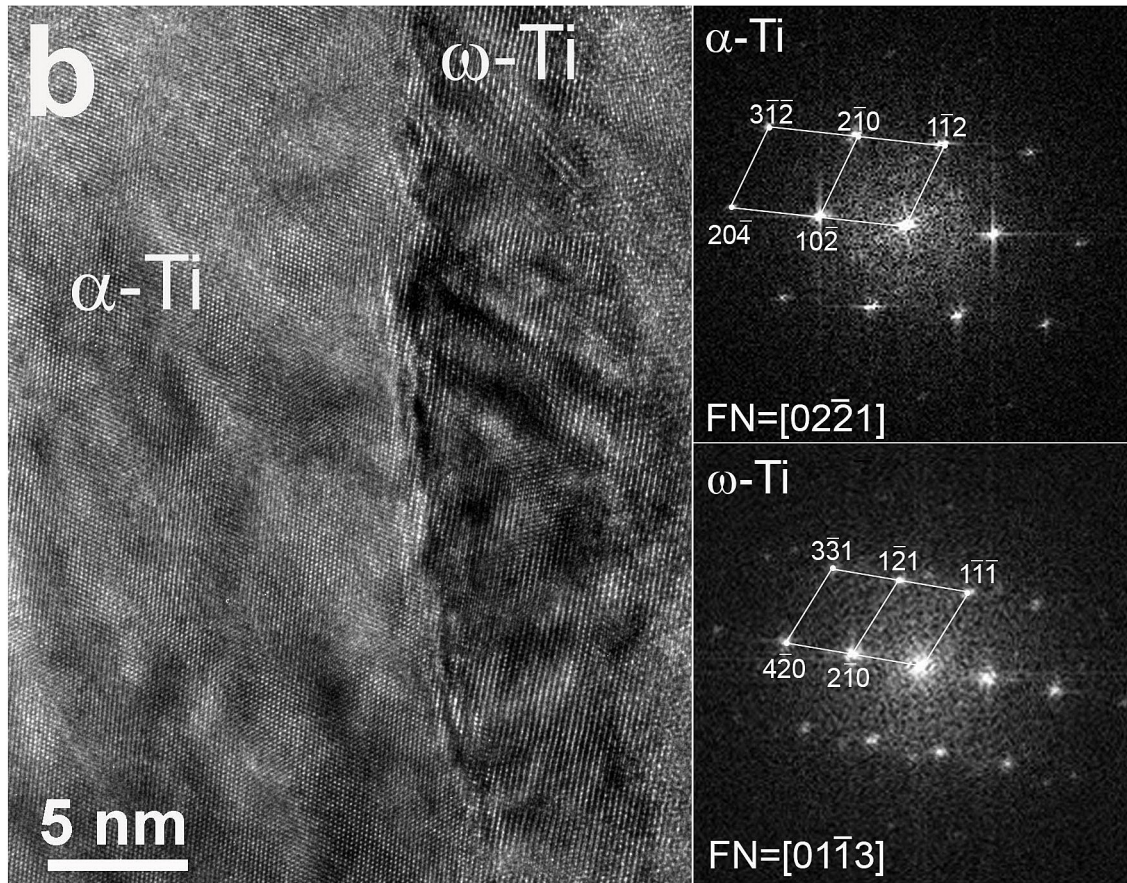
Fig. 7. (*continued*).

4.3. HPT-induced mass transfer

During HPT a certain mass transfer takes place. Previously, we estimated its rate using the differences in the distribution of alloying element between matrix and precipitates before and after HPT [18,21,38]. After HPT the grain size in studied Ti − Fe alloys is about 50—100 nm (Fig. 3a and b). The iron and titanium atoms are distributed uniformly in the samples after HPT in the steady-state (5 rot, $t = 5$ min). Thus, one can use the grain size of $L = 50$ nm as bottom estimation for the distance of HPT-driven mass-transfer. The coefficient of conventional bulk diffusion D for diffusion during duration t for the distance L can be roughly estimated as $D = L^2/t$ [93]. The values of $L = 50$ nm and $t = 300$ s give $D \sim 10^{-17}$ m^2/s. In other words, the HPT-driven mass-transfer in our case is equivalent to the lattice bulk diffusion with $D \sim 10^{-17}$ m^2/s. This is equivalent to the bulk self-diffusion in titanium at 1000 K [94] and to the iron bulk diffusion in titanium at 600 K [95]. The extrapolation to the temperature of HPT treatment $T_{HPT} = 300$ K gives the values of bulk self-diffusion in Ti of $D \sim 10^{-35}$ m^2/s and for the Fe bulk diffusion in Ti of $D \sim 10^{-28}$ m^2/s. We can see that the HPT-driven mass-transfer proceeds very fast. The respective diffusion coefficients D_{HPT} are many orders of magnitude higher than the D values for the conventional bulk diffusion at the temperature of HPT treatment (300 K). And this is despite of the fact that the applied pressure of 6 GPa additionally slows down both bulk diffusion as well as grain boundary migration [96,97]. To be noted, numerous studies have been made to explain so-called anomalous diffusion in β-stabilized alloys of the IVB group of transition metals, which could form ω-phase [98—100]. According to the phenomenological model of anomalous diffusion [99] and neutron scattering experiments [100], it was revealed that the atomic jumps into nearest-neighbour vacancies strongly facilitate the tendency of the bcc lattice of β-phase to fluctuate towards an ω-like structural embryos. Assuming that these localized ω-embryos are presented in the β-phase as structural fluctuations, one expects their concentration to enhance β→ω transition as well as induced diffusion at low temperatures. In such a way, the HPT-driven high steady-state concentration of lattice defects [101—104] appears to be a clue factor of the accelerated mass transfer.

Thus, at 4 wt % Fe the β→ω phase transformation does not need mass-transfer and is, therefore, martensitic. At other concentrations of iron the very fast HPT-driven diffusion-like mass-transfer takes places. The respective diffusion coefficients D_{HPT} are many orders of magnitude higher than the D values for the conventional bulk diffusion at the temperature of HPT treatment (300 K).

4.4. Diffusionless and diffusive paths of the α/β → ω phase transformation

We annealed the Ti − 4 wt % Fe samples at three different temperatures, namely 950, 800 and 620 °C. Thus, we produced three different "initial" states for HPT sample. After annealing at 950 °C in the one-phase β area of the Ti−Fe phase diagram and subsequent quenching, the Ti − 4 wt % Fe alloy contained solely β-phase (Fig. 1a, bottom curve). As we mentioned above, 4 wt % Fe is the optimum concentration for the lattice matching between β - and ω-phases. And we can see that the β→ω transition in this sample proceeds during HPT completely and very quickly. Already

after 0.1 rot. the sample contained almost only ω-phase (see the middle curve in Fig. 1a). It is because no mass transfer is needed for the β→ω transition, and it can proceed via martensitic or diffusionless mechanism.

Oppositely, the Ti–4 wt % Fe samples annealed at 800 °C and 620 °C, namely in the two-phase α+β area of the Ti–Fe phase diagram, and subsequently quenched contained the mixture of α- and β-phases (Fig. 1b, bottom curve). In full accordance with the phase diagram, the α-phase in such samples is almost free from iron. Therefore, all iron atoms are diluted in β-phase. As a result it contains much more iron than the mean concentration in an alloy of 4 wt % Fe. Thus, if the sample contains a mixture of α- and β-phases, the mass transfer is needed for the β→ω transition. As a result, the ω-phase appears only after significant HPT strain (see the middle curve in Fig. 1b) and β→ω transition takes more time.

Consider now the subtle structural features of the (diffusionless and/or diffusion-controlled) transformations of β to ω phase during HPT. The TEM data obtained on samples of Ti–4 wt % Fe alloy annealed at $T = 800$ °C, 270 h, quenched and subjected to HPT for 0.1 anvil rotations are especially valuable for this purpose. In the initial state this sample contained α- and β-phases in the volume ratio about 1:4. After HPT for 0.1 rot. the majority of β-phase transformed to ω phase (Fig. 1a). Fig. 4 shows the α-grain surrounded by a layer of β-phase which is embedded in turn in the ω-matrix. Basing in this picture we can suppose that during HPT the β-phase first transforms into ω-phase. The front of this β→ω transformation moves towards the remaining α-particles. As a result, we can see in Fig. 4 how the thin envelope of β-phase still covers the α-particle. During this process the iron content in the newly-formed ω-phase becomes lower than in initial β-phase. The iron content in the newly-formed ω-phase changes towards the "optimal" one of 4 wt % Fe. On the other hand, it means that in this case the β→ω transformation during HPT requires mass transfer and cannot be purely martensitic. It seems that all β-phase containing about 4.5 wt % Fe easily transformed into ω-phase. However, we observe that the β-phase "envelope" surrounding the particle of α-phase contains more iron (about 6 wt % Fe). Most probably, the additional iron migrated from the iron-free α-particle. The β-phase with 6 wt % Fe has worse lattice matching with ω-phase in comparison with β-phase containing 4 wt % Fe. This fact explains why the β-phase "envelope" around particle of α-phase remains non-transformed. Thus, before HPT the sample annealed at 800 °C and quenched contained the mixture of α- and β-phases with different iron content. However, after five HPT rotations the "final" ω-phase forms which is uniform and contains everywhere 4 wt % Fe, independently on starting state (Fig. 3 TEM, Fig. 1, XRD).

The HRTEM image and respective FFTs in Fig. 5 show the mutual arrangement of lattices of α-grain (area 1) surrounded by a layer of β-phase (area 2) which is embedded in turn in the ω-matrix (area 3). The martensitic OR between β and ω phases is observed: $\{111\}_\beta \| (0001)_\omega; \langle 1\bar{1}0 \rangle_\beta \| \langle 11\bar{2}0 \rangle_\omega$ [6,79]. For this OR three equivalent positions of ω-grains are possible for each β-grain. It can be observed in Fig. 5: namely, the FFT for area 3 (ω-phase) contains all three possible film normals. In other words, the area 3 contains three families of equivalent ω-grains. These equivalent ω-grains have the low-energy "quasi-twin" misorientations among them. This fact supports the idea that the diffusionless martensitic β→ω transformation took place in this sample. On the other hand, no special OR between α and ω-phases corresponding to the known OR 1 $(0001)_\alpha \| (01\bar{1}1)_\omega; \langle 11\bar{2}0 \rangle_\alpha \| \langle 1\bar{1}01 \rangle_\omega$ and OR 2 $(0001)_\alpha \| (11\bar{2}0)_\omega; \langle 11\bar{2}0 \rangle_\alpha \| \langle 0001 \rangle_\omega$ [6] was detected. Also, no special OR between α and β-phases was detected like $(0001)_\alpha \| (110)_\beta; \langle 11\bar{2}0 \rangle_\alpha \| \langle 111 \rangle_\beta$ [63–71]. It means that the HPT-

driven transformations between α and β-phases as well as between α- and ω-phases are diffusional (non-martensitic) and should include mass-transfer.

In any case, after five anvil rotations (i.e. "deep" in the steady state) the state in all three samples is the same, independently on the starting state. They contain almost 95% of ω-phase (Fig. 2a). Similar behavior we observed also for alloys with 2 wt % Fe and 1 wt % Fe (Fig. 2a). Therefore, the state of the Ti–Fe samples after 5 anvil rotation can be determined as "equifinal". In previous works we observed that the composition and structure of phases during HPT in the steady-state is controlled by the dynamic equilibrium between defect formation during SPD and relaxation (or annihilation) of these defects [18,21,38]. The authors of Refs. [101–104] succeeded to observe the extremely high concentration of vacancies in the steady-state during HPT. We found also that in many cases the composition and structure of phases during HPT in this steady-state depends on HPT conditions like pressure, temperature and strain rate. However, they do not depend on the starting state of the sample before HPT (for example, on the composition and morphology of phases). Thus, such steady-state is a kind of *attractor* and can be called *equifinal* following von Bertalanffi [105]. The important difference between the systems called closed and open is that closed systems evolve with time towards *equilibrium* state. The equilibrium state does not depend on the starting state (i.e. before evolution process starts). Analogously, the open systems tend to seek the sustained *equifinal* state, which is also independent on starting one [105].

Thus, the composition and structure of phases in the HPT steady-state does not depend on that in the initial (starting state) before HPT. It is, therefore, equifinal. To the contrary, the path from the initial to equifinal state depends from the starting state. It can include the phase transformations with and without mass-transfer.

4.5. Structural details of the ω phase formation

Iron is an important alloying component in numerous Ti-based alloys with excellent mechanical strength and superior plasticity [106,107]. We saw in Section 4.4 that if the composition of β-phase is close to 4 wt % Fe, the lattice matching between β- and ω-phases is optimal for the β to ω transformation. It takes place without mass transfer and is, therefore, quick and easy. However, if the composition of β-phase differs from 4 wt % Fe, the mass transfer is needed before the martensitic β to ω transformation can happen. In other words, β-phase should first obtain the missing iron atoms or to remove the superfluous ones. If total iron concentration is close to 4 wt % Fe, the iron-rich β-phase and iron-free α-phase can react and form β-phase with 4 wt % Fe which then easily transforms into ω phase. However, if the total iron content is below 4 wt % Fe, the surplus of α-phase remains. It should transform into ω phase "by itself", i.e. like in pure titanium, without help of iron atoms. This case is analysed in Figs. 3 and 4.

The Ti–2 wt % Fe alloy annealed at $T = 800$ °C, 270 h, subsequently quenched and subjected to HPT for 0.1 rot. (Fig. 6 a,b) has layered structure with alternating Fe-enriched and Fe-depleted layers. They correspond to the layers of originally β-phase and originally α-phase. The phase map shows that the HPT-driven formation of "new" ω-phase took place both in Fe-rich and Fe-poor layers. As a result, the sample contains after 0.1 rot. the areas of ω-phase with two different concentrations of iron. The ω-phase transformed from the β-phase contains more iron than the ω-phase transformed from the α-phase. Moreover, the ω-phase transformed from the β-phase contains less iron than the original β-phase. Similarly, ω-phase transformed from the α-phase contains more iron than the original α-phase. Thus, the iron concentrations in ω-grains originated from α- and β-phases "come together" during

HPT. They "meet in a middle point" and in the steady state after 5 rot. the iron concentration becomes uniform and equal to the nominal one of 2 wt % Fe.

HREM micrographs and FFT patterns of this alloy witness that (Fig. 7a):

■ between β- and ω-phase exists the usual OR $\{111\}_\beta \| (0001)_\omega; \langle 1\bar{1}0 \rangle_\beta \| \langle 11\bar{2}0 \rangle_\omega$ [6,79].

■ between α- and ω-phase exists the OR 1 $(0001)_\alpha \| (01\bar{1}1)_\omega; \langle 11\bar{2}0 \rangle_\alpha \| \langle 1\bar{1}01 \rangle_\omega$ [3,6].

On the other hand, one can find locations where abutting α- and ω-grains do not belong to any known OR (Fig. 7b). It means that in case if the total iron concentration differs from the optimal one of 4 wt % Fe, the formation of ω-phases can proceed martensitically both from β-and α-phases. However, the diffusional transformation is not excluded. Moreover, most probably, the diffusion-like redistribution of iron should take place first in order to create the good conditions for the following martensitic transformations.

5. Conclusions

The effect of alloying of titanium with iron (up to 10 wt % Fe) on the ω phase formation during high pressure torsion was studied using XRD analysis, high resolution and orientation imaging TEM. During shear deformation under uniaxial pressure, a pronounced orientation relationship between adjacent grains of α- and ω-phases is accompanied by a strong local preferred orientation, which is recognized as a "basal" crystallographic texture in α-phase. It appears favorable for the realization of the α→ω transformation under HPT conditions.

The amount of retained ω-phase after HPT depends on the iron concentration. In alloys containing β-phase, the addition of iron to titanium changes the lattice matching between β- and ω-phases, and their best conformity makes easier the β→ω phase transformations in comparison with pure Ti. The best matching between β and ω lattices is at 4 wt % Fe. The β→ω phase transformation at 4 wt % Fe does not need mass-transfer and is, therefore, martensitic. At other concentrations of iron the very fast HPT-driven diffusion-like mass-transfer takes places. The respective diffusion coefficients D_{HPT} are many orders of magnitude higher than the D values for the conventional bulk diffusion at the temperature of HPT treatment (300 K).

HPT-driven α→ω and β→ω phase transformations can be distinguished at early-stage deformation due to primarily different solubility of iron in the precursory α- and β-phases respectively. Formation of the almost free of iron ω-phase implies α→ω transition and creates conditions for subsequent redistribution of iron atoms between iron rich and iron depleted ω-phase under HPT influence. Rather homogeneous distribution of iron takes place in the ω-phase at the HPT steady state. Thus, a reduction of the ω-phase volume fraction at the concentrations higher than 4 wt % Fe is caused by the decrease of the α-phase content in the initial states as well as by more pronounced lattice mismatch between β- and ω-phases.

Acknowledgments

References

[1] M.J. Donachie Jr., Titanium: a Technical Guide, second ed., ASM International, Materials Park, OH, USA, 2000.

[2] D. Errandonea, Y. Meng, M. Somayazulu, D. Häusermann, Pressure-induced alpha -> omega transition in titanium metal: a systematic study of the effects of uniaxial stress, Phys. B 355 (2005) 116–125.

[3] D.R. Trinkle, R.G. Hennig, S.G. Srinivasan, D.M. Hatch, M.D. Jones, H.T. Stokes, R.C. Albers, J.W. Wilkins, New mechanism for the alpha to omega martensitic transformation in pure titanium, Phys. Rev. Lett. 91 (2003) 025701.

[4] S.K. Sikka, Y.K. Vohra, R. Chidambaram, Omega-phase in materials, Prog. Mater. Sci. 27 (1982) 245–310.

[5] S. Banerjee, P. Mukhopadhyay, Phase Transformations: Examples from Titanium and Zirconium Alloy, Elsevier, Amsterdam, 2010.

[6] B.S. Hickman, The Formation of omega phase in Ti and Zr alloys: a review, J. Mater. Sci. 4 (1969) 554–563.

[7] Scientific Group Thermodata Europe (SGTE), Thermodynamic Properties of Inorganic Materials,, Landolt-börnstein Group IV (Physical Chemistry), Vol. 19, Subvolume B Binary Systems, Part 3 Binary Systems from Cs-K to Mg-Zr, Springer, Berlin/Heidelberg, 2005.

[8] S.C. Gupta, K.D. Joshi, S. Banerjee, Experimental and theoretical investigations on d and f electron systems under high pressure, Metall. Mater. Trans. A 39 (2008) 1593–1601.

[9] R. Hennig, D.R. Trinkle, J. Bouchet, S.G. Srinivasan, R.C. Albers, J.W. Wilkins, Impurities block the alpha to omega martensitic transformation in titanium, Nat. Mater 4 (2005) 129–133.

[10] N.S. Afonikova, V.F. Degtyareva, Y.A. Litvin, A.G. Rabinkin, Y.A. Skakov, Superconductivity and crystal structure of Ti-Nb alloys after high-pressure action up 120 kbar, Sov. Phys. Sol. State 15 (1973) 746–749.

[11] Y.K. Vohra, S.K. Sikka, E.S.K. Menon, R. Krishnan, High-pressure studies on a prototype omega forming alloy system, Acta Metall. 29 (1981) 457–470.

[12] G.K. Dey, R. Tewari, S. Banerjee, G. Jyoti, S.C. Gupta, K.D. Joshi, S.K. Sikka, Formation of a shock deformation induced omega phase in Zr20Nb alloy, Acta Mater 52 (2004) 5243–5254.

[13] R.Z. Valiev, R.K. Islamgaliev, I. Alexandrov, Bulk nanostructured materials from severe plastic deformation, Progr. Mater. Sci. 45 (2000) 103–189.

[14] B. Straumal, A. Korneva, P. Zięba, Phase transitions in metallic alloys driven by the high pressure torsion, Arch. Civ. Mech. Eng. 14 (2014) 242–249.

[15] W. Lojkowski, M. Djahanbakhsh, G. Burkle, S. Gierlotka, W. Zielinski, H.J. Fecht, Nanostructure formation on the surface of railway tracks, Mater. Sci. Eng. A 303 (2001) 197–208.

[16] V.G. Gavriljuk, Decomposition of cementite in pearlitic steel due to plastic deformation, Mater. Sci. Eng. A 345 (2003) 81–89.

[17] X. Sauvage, F. Wetscher, P. Pareige, Mechanical alloying of Cu and Fe induced by severe plastic deformation of a Cu−Fe composite, Acta Mater 53 (2005) 2127–2135.

[18] B.B. Straumal, B. Baretzky, A.A. Mazilkin, F. Phillipp, O.A. Kogtenkova, M.N. Volkov, R.Z. Valiev, Formation of nanograined structure and decomposition of supersaturated solid solution during high pressure torsion of Al−Zn and Al−Mg, Acta Mater 52 (2004) 4469–4478.

[19] A.A. Mazilkin, B.B. Straumal, E. Rabkin, B. Baretzky, S. Enders, S.G. Protasova, O.A. Kogtenkova, R.Z. Valiev, Softening of nanostructured Al−Zn and Al−Mg alloys after severe plastic deformation, Acta Mater 54 (2006) 3933–3939.

[20] B.B. Straumal, S.G. Protasova, A.A. Mazilkin, E. Rabkin, D. Goll, G. Schütz, B. Baretzky, R. Valiev, Deformation-driven formation of equilibrium phases in the Cu−Ni alloys, J. Mater. Sci. 47 (2012) 360–367.

[21] B.B. Straumal, A.R. Kilmametov, Yu.O. Kucheev, L. Kurmanaeva, Yu. Ivanisenko, B. Baretzky, A. Korneva, P. Zięba, D.A. Molodov, Phase transitions during high pressure torsion of Cu−Co alloys, Mater. Lett. 118 (2014) 111–114.

[22] B. Straumal, R. Valiev, O. Kogtenkova, P. Zieba, T. Czeppe, E. Bielanska, M. Faryna, Thermal evolution and grain boundary phase transformations in severe deformed nanograined Al−Zn alloys, Acta Mater 56 (2008) 6123–6131.

[23] C.M. Cepeda-Jiménez, J.M. García-Infanta, A.P. Zhilyaev, O.A. Ruano, F. Carreño, Influence of the thermal treatment on the deformation-induced precipitation of a hypoeutectic Al−7 wt% Si casting alloy deformed by high-pressure torsion, J. Alloys Comp. 509 (2011) 636–643.

[24] Y. Ivanisenko, W. Lojkowski, R.Z. Valiev, H.J. Fecht, The mechanism of formation of nanostructure and dissolution of cementite in a pearlitic steel during high pressure torsion, Acta Mater 51 (2003) 5555–5570.

[25] B.B. Straumal, A.A. Mazilkin, S.G. Protasova, S.V. Dobatkin, A.O. Rodin, B. Baretzky, D. Goll, G. Schütz, Fe−C nanograined alloys obtained by high pressure torsion: structure and magnetic properties, Mater. Sci. Eng. A 503 (2009) 185–189.

[26] V.V. Sagaradze, V.A. Shabashov, Deformation-induced anomalous phase transformations in nanocrystalline FCC Fe−Ni based alloys, Nanostruct. Mater 9 (1997) 681–684.

[27] S. Ohsaki, S. Kato, N. Tsuji, T. Ohkubo, K. Hono, Bulk mechanical alloying of Cu−Ag and Cu/Zr two-phase microstructures by accumulative roll-bonding process, Acta Mater 55 (2007) 2885–2895.

[28] B.B. Straumal, S.V. Dobatkin, A.O. Rodin, S.G. Protasova, A.A. Mazilkin, D. Goll,

B. Baretzky, Structure and properties of nanograined Fe–C alloys after severe plastic deformation, Adv. Eng. Mater 13 (2011) 463–469.

[29] A.V. Sergueeva, C. Song, R.Z. Valiev, A.K. Mukherjee, Structure and properties of amorphous and nanocrystalline NiTi prepared by severe plastic deformation and annealing, Mater. Sci. Eng. A 339 (2003) 159–165.

[30] S.D. Prokoshkin, I.Yu. Khmelevskaya, S.V. Dobatkin, I.B. Trubitsyna, E.V. Tatyanin, V.V. Stolyarov, E.A. Prokofiev, Alloy composition, deformation temperature, pressure and post-deformation annealing effects in severely deformed Ti-Ni based shape memory alloys, Acta Mater 53 (2005) 2703–2714.

[31] X. Sauvage, L. Renaud, B. Deconihout, D. Blavette, D.H. Ping, K. Hono, Solid state amorphization in cold drawn Cu/Nb wires, Acta Mater 49 (2001) 389–394.

[32] T. Miyazaki, D. Terada, Y. Miyajima, C. Suryanarayana, R. Murao, Y. Yokoyama, K. Sugiyama, M. Umemoto, T. Todaka, N. Tsuji, Synthesis of non-equilibrium phases in immiscible metals mechanically mixed by high pressure torsion, J. Mater. Sci. 46 (2011) 4296–4301.

[33] A.A. Mazilkin, G.E. Abrosimova, S.G. Protasova, B.B. Straumal, G. Schütz, S.V. Dobatkin, A.S. Bakai, Transmission electron microscopy investigation of boundaries between amorphous "grains" in $Ni_{50}Nb_{20}Y_{30}$ alloy, J. Mater. Sci. 46 (2011) 4336–4342.

[34] B.B. Straumal, A.A. Mazilkin, S.G. Protasova, D. Goll, B. Baretzky, A.S. Bakai, S.V. Dobatkin, Formation of two amorphous phases in the $Ni_{60}Nb_{18}Y_{22}$ alloy after high pressure torsion, Kov. Mater. – Metall. Mater 49 (2011) 17–22.

[35] A.M. Glezer, M.R. Plotnikova, A.V. Shalimova, S.V. Dobatkin, Severe plastic deformation of amorphous alloys: I. Structure and mechanical properties, Bull. Russ. Ac. Sci. Phys. 73 (2009) 1233–1236.

[36] G.E. Abrosimova, A.S. Aronin, S.V. Dobatkin, S.D. Kaloshkin, D.V. Matveev, O.G. Rybchenko, E.V. Tatyanin, I.I. Zverkova, The formation of nanocrystalline structure in amorphous Fe-Si-B alloy by severe plastic deformation, J. Metastab. Nanocryst. Mater 24 (2005) 69–72.

[37] P. Henits, Á. Révész, A.P. Zhilyaev, Zs. Kovács, Severe plastic deformation induced nanocrystallization of melt-spun $Al_{85}Y_8Ni_5Co_2$ amorphous alloy, J. Alloys Comp. 461 (2008) 195–199.

[38] B.B. Straumal, V. Pontikis, A.R. Kilmametov, A.A. Mazilkin, S.V. Dobatkin, B. Baretzky, Competition between precipitation and dissolution in Cu–Ag alloys under high pressure torsion, Acta Mater 122 (2017) 60–71.

[39] S.D. Prokoshkin, I.Yu. Khmelevskaya, S.V. Dobatkin, I.B. Trubitsyna, E.V. Tatyanin, V.V. Stolyarov, E.A. Prokofiev, Alloy composition, deformation temperature, pressure and post-deformation annealing effects in severely deformed Ti-Ni based shape memory alloys, Acta Mater 53 (2005) 2703–2714.

[40] C.X. Huang, G. Yang, Y.L. Gao, S.D. Wu, S.X. Li, Investigation on the nucleation mechanism of deformation-induced martensite in an austenitic stainless steel under severe plastic deformation, J. Mater. Res. 22 (3) (2007) 724–729.

[41] T. Waitz, W. Pranger, T. Antretter, F.D. Fischer, H.P. Karnthaler, Competing accommodation mechanisms of the martensite in nanocrystalline NiTi shape memory alloys, Mater. Sci. Eng. A 481–482 (1–2C) (2008) 479–483.

[42] S. Jiang, Y. Zhang, L. Zhao, Y. Zheng, Influence of annealing on NiTi shape memory alloy subjected to severe plastic deformation, Intermetallics 32 (2013) 344–351.

[43] Yu. Ivanisenko, A. Kilmametov, H. Roesner, R.Z. Valiev, Evidence of α → ω phase transition in titanium after high pressure torsion, Int. J. Mater. Res. 99 (2008) 36–41.

[44] B.B. Straumal, A.R. Kilmametov, G.A. López, I. López-Ferreño, M.L. Nó, J. San Juan, H. Hahn, B. Baretzky, High-pressure torsion driven phase transformations in Cu–Al–Ni shape memory alloys, Acta Mater 125 (2017) 274–285.

[45] B.B. Straumal, A.R. Kilmametov, Yu. Ivanisenko, A.S. Gornakova, A.A. Mazilkin, M.J. Kriegel, O.B. Fabrichnaya, B. Baretzky, H. Hahn, Phase transformations in Ti-Fe alloys induced by high pressure torsion, Adv. Eng. Mater 17 (2015) 1835–1841.

[46] Y. Ivanisenko, A. Kilmametov, H. Roesner, R.Z. Valiev, Evidence of alpha ->omega phase transition in titanium after high pressure torsion, Int. J. Mater. Res. 99 (2008) 36–41.

[47] B.B. Straumal, A.S. Gornakova, A.A. Mazilkin, O.B. Fabrichnaya, M.J. Kriegel, B. Baretzky, J.–Z. Jiang, S.V. Dobatkin, Phase transformations in the severely plastically deformed Zr–Nb alloys, Mater. Lett. 81 (2012) 225–228.

[48] R.Z. Valiev, Nanostructuring of metals by severe plastic deformation for advanced properties, Nat. Mater 3 (2004) 511–516.

[49] R.Z. Valiev, I.V. Alexandrov, Y.T. Zhu, T.C. Lowe, Paradox of strength and ductility in metals processed by severe plastic deformation, J. Mater. Res. 17 (2002) 5–8.

[50] L.-C. Zhang, Mechanical properties of titanium-based alloys, Adv. Mater. Res. 1 (2012) 13–18.

[51] D.V. Louzguine, H. Kato, L.V. Louzguina, A. Inoue, High-strength binary Ti–Fe bulk alloys with enhanced ductility, J. Mater. Res. 19 (2004) 3600–3606.

[52] M. Koike, Ch. Ohkubo, H. Sato, H. Fujii, T. Okabe, Evaluation of cast Ti-Fe-O-N alloys for dental applications, Mater. Sci. Eng. C 25 (2005) 349–356.

[53] B. Völker, N. Jäger, M. Calin, M. Zehetbauer, J. Eckert, A. Hohenwarter, Influence of testing orientation on mechanical properties of Ti45Nb deformed by high pressure torsion, Mater. Des. 114 (2017) 40–46.

[54] A. Panigrahi, B. Sulkowski, Th. Waitz, K. Ozaltin, W. Chrominski, A. Pukenas, J. Horky, M. Lewandowska, W. Skrotzki, M. Zehetbauer, Mechanical properties,structural and texture evolution of biocompatible Ti–45Nb alloy

processed by severe plastic deformation, J. Mech. Behav. Biomed. Mater 62 (2016) 93–105.

[55] R. Davis, H.M. Flower, D.R.F. West, Martensitic transformations in Ti-Mo alloys, J. Mater. Sci. 14 (1979) 712–722.

[56] R.Z. Valiev, Yu.V. Ivanisenko, E.F. Rauch, B. Baudelet, Structure and deformation behaviour of armco iron subjected to severe plastic deformation, Acta Metall. 44 (1996) 4705–4712.

[57] A.V. Korznikov, G. Tram, O. Dimitrov, G.F. Korznikova, S.R. Idrisova, Z. Pakiela, The mechanism of nanocrystalline structure formation in Ni_3Al during severe plastic deformation, Acta Mater 49 (2001) 663–671.

[58] M. Wojdyr, Fityk: a general-purpose peak fitting program, J. Appl. Cryst. 43 (2010) 1126–1128.

[59] J.-J. Fundenberger, A. Morawiec, E. Bouzy, Advances in automatic TEM based orientation mapping, Solid State Phenom. 105 (2005) 37–42.

[60] A. Kobler, A. Kashiwar, H. Hahn, C. Kübel, Combination of in situ straining and ACOM TEM: a novel method for analysis of plastic deformation of nanocrystalline metals, Ultramicroscopy 128 (2013) 68–81.

[61] J.L. Lábár, Consistent indexing of a (set of) SAED pattern(s) with the ProcessDiffraction program, Ultramicroscopy 103 (2005) 237–249.

[62] A. Kilmametov, Yu. Ivanisenko, B. Straumal, A.A. Mazilkin, A.S. Gornakova, M.J. Kriegel, O.B. Fabrichnaya, D. Rafaja, H. Hahn, Transformations of α' martensite in Ti-Fe alloys under high pressure torsion, Scr. Mater 136 (2017) 46–49.

[63] W. Pitsch, A. Schrader, The shape of precipitation of the ε carbide in the ferrite and in the martensite during tempering, Arch. Eisenhüttenwes 29 (1958) 715–721.

[64] U. Dahmen, Orientation relationships in precipitation systems, Acta Metall. Mater 30 (1982) 63–73.

[65] H. Kaneko, Y.C. Huang, Martensitic transformations in binary titanium alloys, J. Jpn. Inst. Met. 27 (1963) 1393–1399.

[66] V.N. Moiseev, Properties and heat treatment of Ti–Fe and Ti–Fe–Al alloys, Met. Sci. Heat. Treat. 11 (1969) 335–339.

[67] T. Sato, S. Hukai, Y.C. Huang, The M_s points of binary titanium alloys, J. Austral. Inst. Met. 5 (2) (1960) 149–153.

[68] P. Duwez, The martensite transformation in titanium binary alloys, Trans. Am. Soc. Met. 45 (1953) 934–940.

[69] D.H. Polonis, J.G. Parr, The β-α transformation in titanium, Trans. Am. Inst. Min. Met. Eng. 200 (1954) 1148–1154.

[70] Y.N. Gridnev, Yu.N. Petrov, V.A. Rafalovskiy, The martensite transformation in titanium, Vopr. Fiz. Met. Metalloved. AN UkrSSR Sb. Nauchn. Rabot 11 (1960) 82–90 (In Russian).

[71] J.L. Murray, Evaluation of titanium phase diagram, Bull. Alloy Phase Diagr. 2 (1981) 32–40.

[72] G.A. López, E.J. Mittemeijer, B.B. Straumal, Grain boundary wetting by a solid phase; microstructural development in a Zn–5 wt.% Al alloy, Acta Mater 52 (2004) 4537–4545.

[73] A.S. Gornakova, S.I. Prokofiev, K.I. Kolesnikova, B.B. Straumal, Formation regularities of grain boundary interlayers of the α-Ti phase in binary titanium alloys, Russ. J. Non-Ferrous Met. 56 (2016) 229–235.

[74] A.S. Gornakova, S.I. Prokofiev, B.B. Straumal, K.I. Kolesnikova, Growth of (αTi) grain boundary layers in Ti–Co alloys, Russ. J. Non-Ferrous Met. 57 (2016) 703–709.

[75] R. Ray, B.C. Giessen, N.J. Grant, The constitution of metastable titanium-rich Ti-Fe alloys: an order-disorder transition, Metall. Trans. 3 (1972) 627–629.

[76] B.W. Levinger, Lattice parameter of beta titanium at room temperature, Trans. Am. Inst. Min. Met. Eng. 197 (1953) 195–200.

[77] S.G. Fedotov, N.F. Kvasova, M.I. Ermolova, Decomposition of the metastable solid solution of titanium with ipron, Dokl. Akad. Nauk. SSSR 216 (2) (1974) 363–366.

[78] L.N. Guseva, L.K. Dolinskaya, Metastable phases in titanium alloys with group VIII elements quenched from the β-Region, Izv. Akad. Nauk. SSSR Met. (6) (1974) 195–202.

[79] U. Zwicker, Titan und Titanlegierungen, Springer, Berlin, 1974.

[80] J.M. Silcock, An x-ray examination of the ω phase in the Ti-V, Ti-Mo, and Ti-Cr alloys, Acta Metall. 6 (1958) 481–493.

[81] D.R. Trinkle, D.M. Hatch, H.T. Stokes, R.G. Hennig, R.C. Albers, Systematic pathway generation and sorting in martensitic transformations: titanium alpha to omega, Phys. Rev. B 72 (2005) 0141051.

[82] L. Beausir, L.S. Toth, K.W. Neale, Ideal orientations and persistence characteristics of hexagonal close packed crystals in simple shear, Acta Mater 55 (2007) 2695–2705.

[83] V. Sitdikov, I. Alexandrov, Texture analysis of ω-phase Ti subjected to high-pressure torsion, Rev. Adv. Mater. Sci. 31 (2012) 85–89.

[84] S. Gatina, I. Semenova, J. Leuthold, R. Valiev, Nanostructuring and phase transformations in the beta-alloy Ti-15Mo during high-pressure torsion, Adv. Eng. Mater 17 (2015) 1742–1747.

[85] Z.Y. Hu, X.W. Cheng, Z.H. Zhang, H. Wang, S.L. Li, G.F. Korznikova, D.V. Gunderov, F.C. Wang, The influence of defect structures on the mechanical properties of Ti-6Al-4V alloys deformed by high-pressure torsion at ambient temperature, Mater. Sci. Eng. A 684 (2017) 1–13.

[86] J. Xu, W. Zeng, Y. Zhao, X. Sun, Z. Du, Influence of cooling rate following heat treatment on microstructure and phase transformation for a two-phase alloy, J. Alloys Comp. 688 (2016) 301–309.

[87] K.-M. Hong, Y.C. Shin, Analysis of microstructure and mechanical properties change in laser welding of Ti6Al4V with a multiphysics prediction model,

J. Mater. Proc. Technol. 237 (2016) 420–429.

[88] J. Yang, H. Yu, J. Yin, M. Gao, Z. Wang, X. Zeng, Formation and control of martensite in Ti-6Al-4V alloy produced by selective laser melting, Mater. Des. 108 (2016) 308–318.

[89] P. Zhao, L. Fu, H. Chen, Low cycle fatigue properties of linear friction welded joint of TC11 and TC17 titanium alloys, J. Alloys Comp. 675 (2016) 248–256.

[90] Q. Zhang, J. Chen, H. Tan, X. Lin, W. Huang, et al., Microstructure evolution and mechanical properties of laser additive manufactured Ti–5Al–2Sn–2Zr–4Mo–4Cr alloy, Trans. Nonferr. Met. Soc. China 26 (2016) 2058–2066.

[91] M.M. Stupel, M. Ron, B.Z. Weiss, Phase identification in titanium-rich Ti–Fe system by Mössbauer spectroscopy, J. Appl. Phys. 47 (1976) 6–12.

[92] F.F. Cardoso, A. Cremasco, R.J. Contieri, E.S.N. Lopes, C.R.M. Afonso, R. Caram, Hexagonal martensite decomposition and phase precipitation in Ti–Cu alloys, Mater. Des. 32 (2011) 4608–4613.

[93] H. Mehrer, Diffusion in Solids. Fundamentals, Methods, Materials, Diffusion-controlled Processes, Springer, Berlin, 2007, p. 651.

[94] J.E. Murdock, T.S. Lundy, E.E. Stansbury, Diffusion of Ti44 and V48 in titanium, Acta Metall. 12 (1964) 1033–1039.

[95] H. Nakajima, M. Koiwa, S. Ono, Diffusion of iron in single crystal α-titanium, Scr. Metall. 17 (1983) 1431–1434.

[96] D.A. Molodov, B.B. Straumal, L.S. Shvindlerman, The effect of pressure on migration of <001> tilt grain boundaries in tin bicrystals, Scr. Metall. 18 (1984) 207–211.

[97] D.A. Molodov, J. Swiderski, G. Gottstein, W. Lojkowski, L.S. Shvindlerman, Effect of pressure on grain boundary migration in aluminium bicrystals, Acta Metall. Mater 42 (1994) 3397–3407.

[98] R.F. Peart, J. Askill, The mechanism of diffusion in b.c.c. transition metals, Phys. Stat. Sol. 23 (1967) 263–275.

[99] J.M. Sanchez, D. De Fontaine, Anomalous diffusion in Omega forming system, Acta Metall. 26 (1977) 1083–1095.

[100] W. Petry, T. Flottmann, A. Heiming, J. Trampenau, M. Alba, Atomistic study of anomalous self-diffusion in bcc β-Titanium, Phys. Rev. Lett. 61 (1988) 722–725.

[101] T. Ungar, E. Schafler, P. Hanak, S. Bernstorff, M. Zehetbauer, Vacancy production during plastic deformation in copper determined by in situ X-ray diffraction, Mater. Sci. Eng. A 462 (2007) 398–401.

[102] T. Ungár, E. Schafler, P. Hanák, S. Bernstorff, M. Zehetbauer, Vacancy concentrations determined from the diffuse background scattering of X-rays in plastically deformed copper, Z. Met. 96 (2005) 578–583.

[103] M.B. Kerber, M. Zehetbauer, E. Schafler, F.C. Spieckermann, S. Bernstorff, T. Ungar, X-ray line profile analysis-An ideal tool to quantify structural parameters of nanomaterials, JOM 63 (2011) 61–69.

[104] A.R. Kilmametov, G. Vaughan, A.R. Yavari, A. LeMoulec, W.J. Botta, R.Z. Valiev, Microstructure evolution in copper under severe plastic deformation detected by in situ X-ray diffraction using monochromatic synchrotron light, Mater. Sci. Eng. A 503 (2009) 10–13.

[105] L. von Bertalanffy, The theory of open systems in physics and biology, Science 111 (1950) 23–29.

[106] V.Yu. Zadorozhnyy, X. Shi, A.N. Kopylov, I.V. Shchetinin, T. Wada, D.V. Louzguine-Luzgin, H. Kato, Mechanical properties, structure, and biocompatibility of dual-axially forged Ti₉₄Fe₃Au₃, Ti₉₄Fe₃Nb₃, and Ti₉₄Au₃Nb₃ alloys, J. Alloys Comp. 707 (2017) 269–274.

[107] G.-H. Zhao, S.V. Ketov, J. Jiang, H. Mao, A. Borgenstam, D.V. Louzguine-Luzgin, New beta-type Ti-Fe-Sn-Nb alloys with superior mechanical strength, Mater. Sci. Eng. A 705 (2017) 348–351.